2013

A secondary monitor unit calculation algorithm using superposition of symmetric, open fields for IMRT plans

Adam Michael Watts
Louisiana State University and Agricultural and Mechanical College, awatts7@lsu.edu

Recommended Citation

Watts, Adam Michael, "A secondary monitor unit calculation algorithm using superposition of symmetric, open fields for IMRT plans" (2013). *LSU Master's Theses*. 1742.
https://digitalcommons.lsu.edu/gradschool_theses/1742

A SECONDARY MONITOR UNIT CALCULATION ALGORITHM USING SUPERPOSITION OF SYMMETRIC, OPEN FIELDS FOR IMRT PLANS

A Thesis

Submitted to the Graduate Faculty of the
Louisiana State University and
Agricultural and Mechanical College
in partial fulfillment of the
requirements for the degree of
Master of Science

in

The Department of Physics and Astronomy

by
Adam Michael Watts
B.S., University of Delaware, 2010
December 2013

Acknowledgment

There are many people who are ultimately responsible for the completion of this project, though only a few are listed here. I thank Dr. John Gibbons, my committee chair. His help and input with the design of the project, execution of measurements, and preparation of the thesis, as well as multiple presentations has taught me much. I thank the members of my supervisory committee, Connel Chu, Dr. Kenneth Matthews, Dr. Alkhatib, and Dr. Shane Stadler for their feedback throughout the project.

Connel Chu’s technical knowledge of the Pinnacle treatment planning system was invaluable. I thank Gordon Mancuso and Dr. Jonas Fontenot for their previous work of performing TG-119 measurements at our institution, a large part of this project was made possible by using their data. I thank Oncology Data Systems, INC for partial funding of the project and the dosimetry staff at Mary Bird Perkins Cancer Center for their help with the planning portion of this project.

I thank my friends for the necessary escapes from the project when needed, especially Nicole for her love and support, and John-Paul for the multiple distractions throughout the program. The support my family has given me cannot be overstated. I would not be at this point if not for the multiple opportunities they have afforded me throughout my life.

Table of Contents

List of Tables

List of Figures

Abstract

Purpose: To perform a secondary dose calculation for intensity modulated radiotherapy (IMRT) or volumetric modulated arc therapy (VMAT) plans to a point on or off axis within 2% using open field data.

Methods: An independent dose calculation algorithm has been developed for complex fields with multiple segments. The algorithm subdivides dose into the contributions from each opposing leaf pair for a given multileaf collimator (MLC) configuration. Leaf pair dose is determined by drawing four rectangular fields based on leaf positions, which are symmetric about the point of calculation. Superposition of these fields yields the dose from the leaf pair to the point. VMAT plans are approximated by a static MLC configuration at four degree intervals. The algorithm requires standard open field data (e.g., head and phantom scatter factors, S_{cp}s and tissue phantom ratios, TPRs), and the MLC control point information. Calculations were done with additional measured small field output factors down to a 1.5x1.5-cm^2 field. Algorithm doses to the isocenter or center of the planning target volume (PTV) were compared with heterogeneous Pinnacle calculations of a series of prostate, head and neck, and chest wall treatment plans. Delivery techniques included fixed gantry IMRT and VMAT.

Results: Good agreement was obtained between doses calculated by the algorithm and the Pinnacle^3 treatment planning system. Percent errors were -0.2% ± 3.8% (mean and 95% confidence interval) for algorithm calculations. Systematic offsets were observed as a function of calculation site, with prostate doses being underestimated and chest wall doses being overestimated. Errors are likely the result of patient geometry deviations from the infinite slab, flat phantom assumption of monitor unit calculations.

Conclusion: Results demonstrate that clinically acceptable agreement is obtained using this method. Further improvement could be made with more accurate heterogeneity correction factors and/or a better estimation of small field output factors.

Chapter 1 : Introduction

1.1 Background and Significance

1.1.1 IMRT treatments

The goal of external radiation therapy is to deliver a tumorcidal dose of radiation to cancerous cells, while minimizing dose to surrounding healthy tissues and critical structures. Traditionally, the majority of radiation treatments use beams of uniform intensity across the field. Wedges or compensators can modify this intensity profile, while blocks can further shape the field. Intensity modulated radiation therapy (IMRT) is a newer technique in which non-uniform intensity profiles are delivered from multiple angles. The composite of these profiles has been optimized to maximize tumor dose, while minimizing dose to surrounding tissues to a higher degree than traditional techniques would allow. An example of each treatment is shown in Figure 1.1.

Two systems make this technique clinically possible, a three-dimensional treatment planning system (TPS) with the ability to calculate dose from and optimize non-uniform fluence patterns, and a method of delivering these planned non-uniform intensity profiles such as a multileaf collimator (MLC).[1] A MLC is a device positioned in the beam line either in addition to or replacing one of the photon collimating jaws. It is made up of multiple opposing leaves with sufficient thickness to attenuate the photon beam to a level approximately 1-2% of the primary beam. These leaves can move perpendicular to the central axis and can be positioned to create desired field patterns. An illustration on a MLC is shown in Figure 1.2 as well as a beam's-eye-view representation that will be commonly used throughout this work.

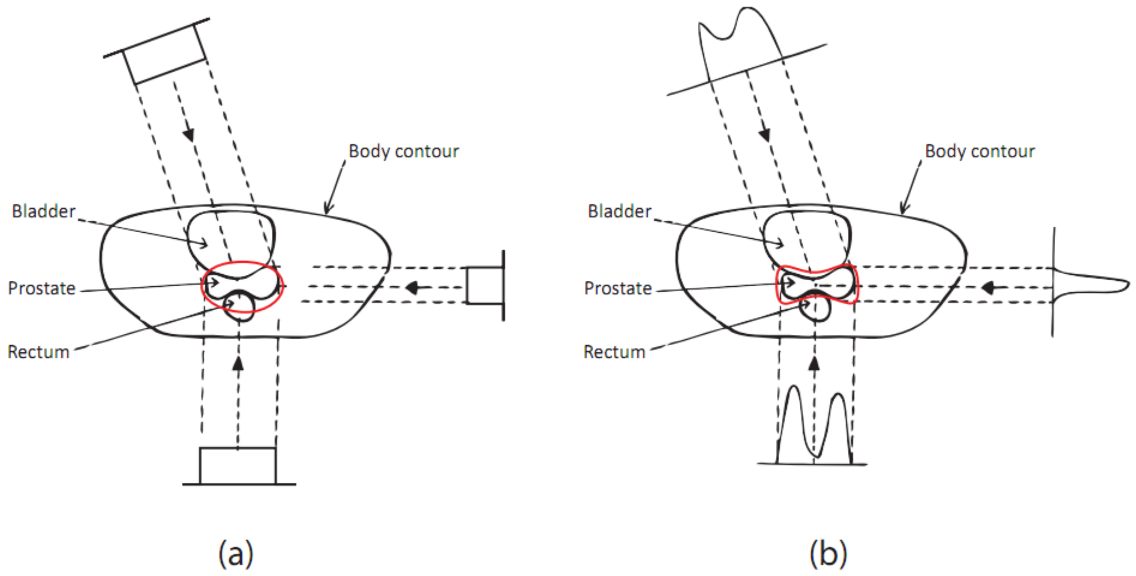

Figure 1.1: Displayed are axial views of a conventional (a) and IMRT (b) treatment plans each with three beams directed towards the prostate at different gantry angles. The red line indicates a representative isodose line for each treatment. Although the field sizes and gantry angles for the beams are equivalent in each case, the intensity profiles displayed at the source of each beam are different, allowing for greater conformity in the IMRT plan. Image adapted from Webb et al.[2]

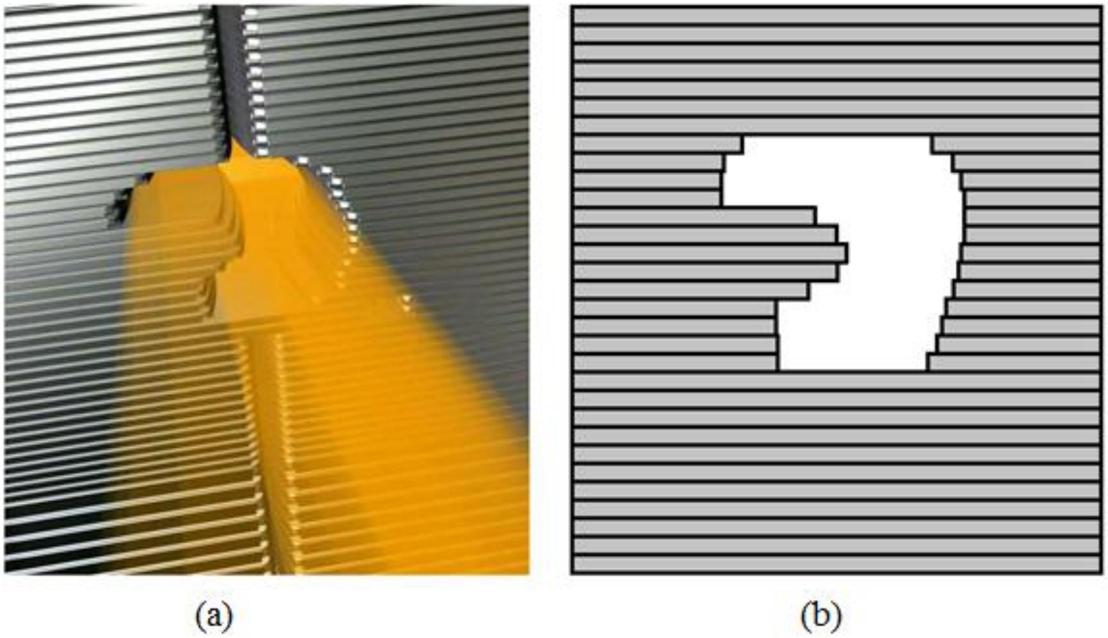

Figure 1.2: Example of an MLC. (a) Illustration of a MLC collimating a beam of radiation to a desired shape. (b) A beam's-eye-view representation of the MLC.

There are a number of different techniques that have been developed for IMRT. This project has focused on the verification of two specific techniques known as segmental multileaf collimation (SMLC or SMLC-IMRT), commonly referred to as “step-and-shoot”, and volumetric modulated arc therapy (VMAT). SMLC plans generally consist of 9 beams at fixed gantry angles spaced around the patient, each with its own optimized fluence distribution. This fluence distribution is created by adding together multiple discrete sub-fields called segments. During delivery, each segment is exposed for a set number of monitor units (MU) defined by a series of control points. In SMLC deliveries, there is no radiation delivered while the MLC transitions between segments.

By contrast, VMAT is a continuous delivery with both the gantry and MLC leaves moving during the delivery of radiation. VMAT treatments consist of one to two arcs over a defined angle around the patient. Radiation is delivered continuously at variable dose rate while MLC leaves, photon jaws, and the gantry are in motion. These variables are optimized as a function of gantry angle during planning to achieve a desired composite dose distribution. VMAT treatments are faster than and exhibit dose distributions equivalent to gantry-static IMRT techniques.[3]

1.1.2 Patient Specific Quality Assurance

Patient specific plan verification has always been a part of quality assurance, with a secondary calculation of dose recommended by multiple sources.[4-8] Conventional treatments were verified by hand calculations of the number of monitor units required to deliver a specified dose to a single calculation point. This method is impractical for IMRT treatments due to irregular field shapes and the large number of segments for each plan. As a result, the current practice is to verify IMRT treatment plans using surrogate phantom measurements. The planned beams are transferred to a CT of a measurement phantom and dose is calculated. The phantom is then irradiated with ion chamber, film, or diode arrays used to measure the dose. Results are compared to the calculated dose in the phantom. This is sufficient for the majority of cases, but there are some errors that will not be caught by measurements, such as failure to remove the couch, incorrect patient data, an incorrect CT-density table, or errors transferring data to the record and verify system.[7] Independent dose calculation methods would catch these errors, provided they do not use information from the treatment planning system for input. Ideally, output from a record and verify system should be used.[7] Phantom measurements might eventually fall out of use as confidence in secondary dose calculations increase.

1.1.3 Current IMRT Dose Verification Algorithms

There multiple approaches in the literature for an independent dose calculation of IMRT plans. [9-17] These range in complexity from Modified Clarkson Integration (MCI) to Monte Carlo techniques. There are currently three commercial products based on these algorithms available: MuCheck, developed by Oncology Data Systems, Inc. (http://mucheck.com/odsweb/), RadCalc, developed by Lifeline Software, Inc. (http://lifelinesoftware.com/index.php), and IMSure, developed by Standard Imaging, Inc. (http://www.standardimaging.com/).

MuCheck and RadCalc are both based on the work of Kung et al.[10] which is a MCI technique. An illustration of the process is shown in Figure 1.3. A delivered fluence grid MU(x,y) is built from MLC sequence files from the treatment planning system. Intensity values for each beamlet are based on leaf open times plus leakage. Assuming radial symmetry of dose, all beamlets r distance from the CAX contribute an equal amount of scatter per monitor unit to the point of calculation. This allows the fluence grid to be averaged over concentric annular sectors and expressed as the weighted sum of these sectors. Dose from an annular field with inner and outer radii of (r, r+Δr) is determined by subtracting a circular field of radius r from a field of radius r+Δr. Dosimetric information of circular fields is obtained by assuming a disk of radius r to have an equivalent square of 2r x 2r. The algorithm was found to be within 3% of values calculated in the Corvus treatment planning system for five SMLC-IMRT plans. This method was originally intended for on-axis calculations in a homogeneous medium, but has since been extended to off-axis calculations in heterogeneous media for commercial use.

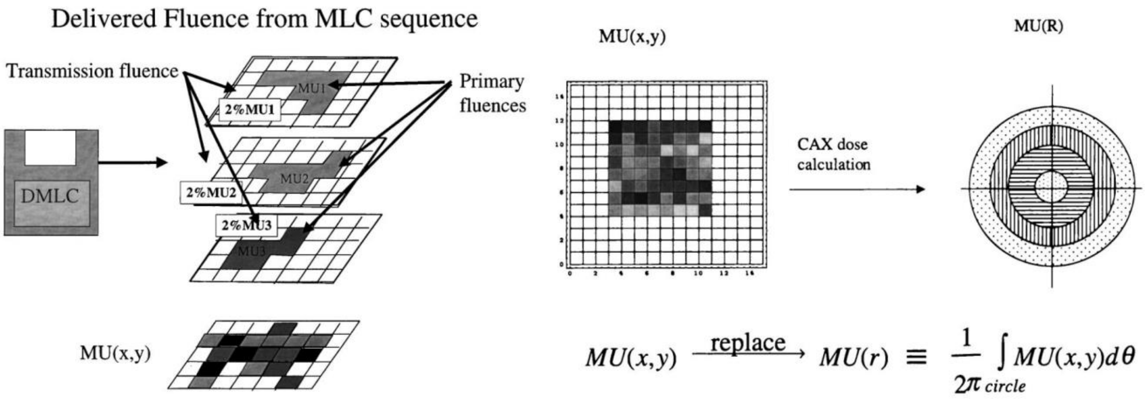

Figure 1.3: Modified Clarkson Integration. The conversion of the MLC sequence to a fluence grid to annular dose sectors. Image adapted from Kung et al.[10]

IMSure is based on work done by Yang et al.[13] which is an extension of the work done by Xing et al.[14] The technique determines point dose by expressing the field as the sum of multiple beamlets, weighted according to fractional amount that beamlet is open for the delivery. Beamlet specific head scatter factors are determined using a three-source model[13] and leakage for closed beamlets is calculated using an average transmission factor. Dose from each beamlet to the point of calculation can be determined by methods ranging from MCI to Monte Carlo simulation. Algorithm calculations at isocenter were within 2% when compared to the Corvus treatment planning system and in-phantom ion chamber measurements for two plans, with higher errors found at off-axis points. Accuracy of this method is highly dependent of the correct determination of beamlet dose.

Monte Carlo methods are the most accurate approaches to dose calculation, however execution time is generally prohibitive especially when used as a patient specific check. Fan et al.[17] developed a Monte Carlo approach using the point detector method and next event estimation. The probability of a photon reaching the point of measurement from each interaction during its random walk is calculated, rather than simply recording energy deposited in the voxel, greatly increasing calculation efficiency. Photon energy fluence at point is determined and converted to collision kerma by the mass energy absorption coefficient. Results were within 2% in low gradient areas for 20 plans when compared to EGS4/MCSIM simulations, with calculations being 20 times faster at around 5 minutes. While impressive, Monte Carlo methods are impractical for implementation in the average clinic due to the complexity of their commissioning process.

1.1.4 TomoTherapy Dose Calculation Algorithm

Helical TomoTherapy is a specialized delivery system that delivers dose in a helical fashion using the same geometry as a CT scanner. For these systems, the fan beam is modulated by a one-dimensional, binary MLC. Gibbons et al.[18] devised a simple, yet accurate method for point dose calculations for the helical TomoTherapy system. A modulated field from a single projection is shown in Figure 1.4(a), the leaf open time for each leaf is shown with leaf number m as the leaf centered over the point of calculation. This projection is approximated by setting leaves $m \pm n$ equal to their average, resulting in the symmetric projection shown in Figure 1.4(b). This symmetric projection may be expressed as the sum of multiple symmetric unmodulated segments 1-4 as shown in Figure 1.4(c). Dose of these fields are determined using traditional hand monitor unit calculation methods that have been modified for the TomoTherapy treatment geometry. Point dose is determined by summing the dose from all projections in the treatment.

Note that some of these segments may have negative treatment times. While this is not physically possible, it is acceptable for dose calculation purposes. The algorithm was used to calculate point doses for a number of patient treatment plans, which were compared with the point doses determined by the TomoTherapy Treatment Planning System (TPS). Agreement between the algorithm and the TPS was within 2% for 94% patient plans (64 of 68) for sites other than the lung or superficial planning target volumes (PTV). These sites showed a systematic overestimation of dose with an average and standard deviation of 3.1% ± 2.4%. This was thought to be due to overestimation of scattering material surrounding the source to point ray.

This algorithm has multiple benefits over previously discussed approaches while still being sufficiently accurate for clinical use. It uses open field data which are measured at time of machine commissioning and is mathematically simple enough to be verified by hand if needed. The dose calculation formalism has been in use for verification of conventional treatments for years and is well understood.

The approach used by Gibbons et al. for helical tomotherapy could be extended to conventional MLC IMRT deliveries, provided a methodology was created to convert the two-dimensional non-uniform fluence matrix into a summation of uniform, symmetric fluence matrices. In this case, the total dose would be computed as a summation of open fields, symmetric about the point of calculation. The algorithm would be able to use dosimetric functions already measured for conventional MU calculations, and would avoid problems calculating doses from small, individual beamlets.

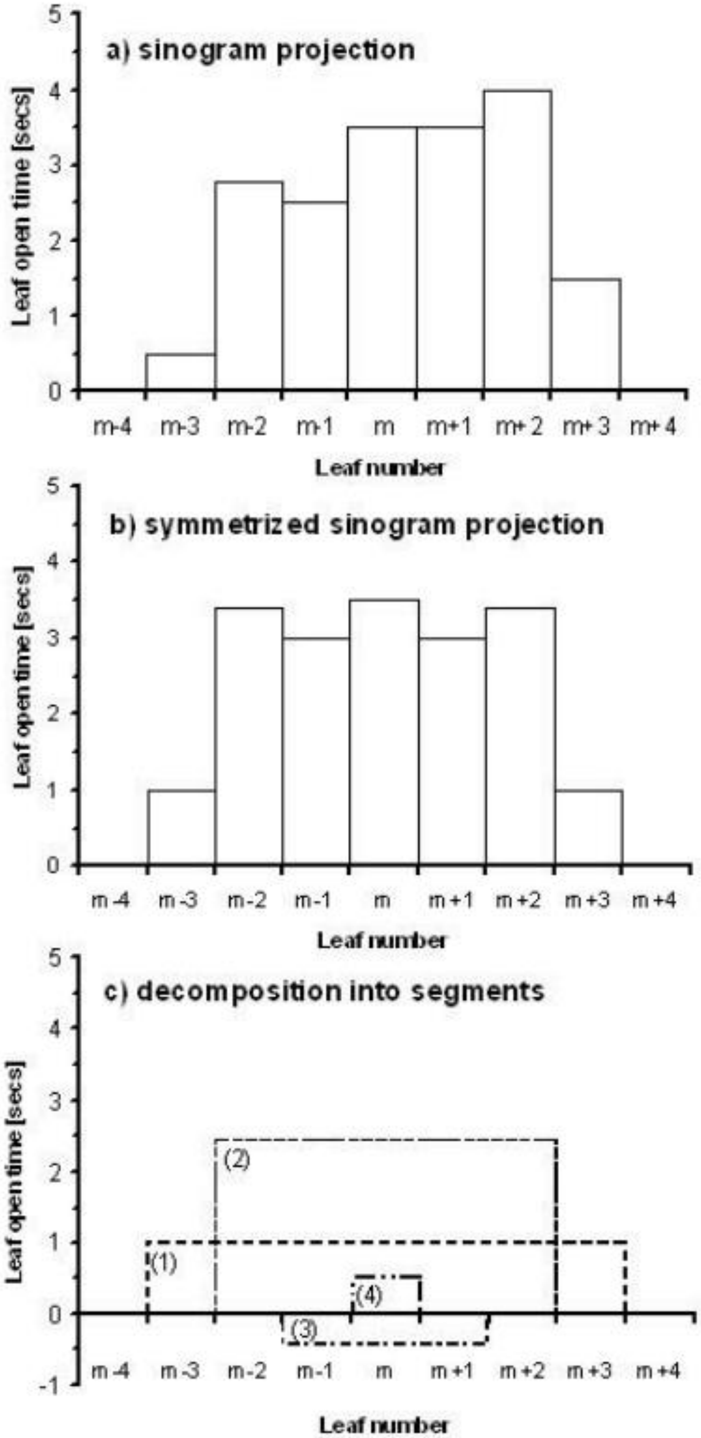

Figure 1.4: Example of TomoTherapy algorithm decomposition of a single projection. The original leaf open projection (a) is symmetrized about leaf m, yielding a symmetric projection (b) that delivers an equivalent amount of dose. This symmetric projection is then expressed as superposition of multiple symmetric segments of unmodulated leaf-open fields (c) which can be calculated using premeasured data. Image from Gibbons et al.[18]

1.2 Hypothesis

An independent monitor unit calculation algorithm using a superposition of open-field data can be used to accurately predict calculated doses for SMLC and VMAT plans to within 2% for points in high-dose low gradient regions.

1.3 Specific Aims

Aim 1: Adapt the TomoTherapy independent dose calculation algorithm for calculation of dose from fields delivered with conventional MLCs.

Aim 2: Obtain dosimetric data as required for input into the algorithm.

Aim 3: Compare the algorithm to Pinnacle calculations and point dose ion chamber measurements of test cases presented in AAPM Report Task Group 119.[19]

Aim 4: Compare the algorithm to Pinnacle calculations of a series of SMLC and VMAT patient plans.

Chapter 2 : Methods and Materials

2.1 Aim 1: Adapt the TomoTherapy Algorithm for Calculation of SMLC and VMAT deliveries

2.1.1 The Algorithm's Approach

As discussed in the introduction, IMRT deliveries use multiple beams with non-uniform fluence, the composite of which has been optimized to give a desired dose distribution in the patient geometry. In the case of SMLC deliveries, these non-uniform fluence distributions are created by adding multiple MLC-defined field configurations, called segments, from the same angle to achieve the result. Segments are defined at the linac by control points, which specifies the state of the machine (e.g., MLC leaf positions, gantry angle, etc.). In the case of VMAT deliveries, the radiation beam is continuously on while the gantry, jaws, and MLC leaves are all in motion. Within the Pinnacle TPS, the VMAT plan is defined by control points placed at regular gantry intervals, typically every four degrees, and a cumulative number of monitor units that have been delivered when the gantry arrives at each of these computer optimized angles and field configurations. In the Pinnacle TPS, the total dose delivered over a four degree arc, centered around the control point, is approximated as being delivered at a single gantry angle defined at the control point.[8] So for dose calculation purposes, both SMLC and VMAT deliveries are represented as the sum of gantry-static segments, each defined by the planned control points. Each control point has its own gantry angle, jaw positions, MLC positions, and number of monitor units (MU) associated with it.

In this approach, we subdivide control point dose per MU into the contributions from each opposing leaf pair gap. Leaf gap dose per MU is determined by the superposition of four fields, symmetric about the point of calculation, whose dimensions are based on the corners of the gap in question. An example beam's-eye-view of a MLC defined control point is shown in

Figure 2.1. In this example, the dose will be calculated to the black dot in the center of the figure. Initially, we are calculating the dose to this point due to the radiation delivered between the blue leaf pair at the top of the figure. The corners of the leaf gap for this leaf pair are labeled as A, B, C, and D.

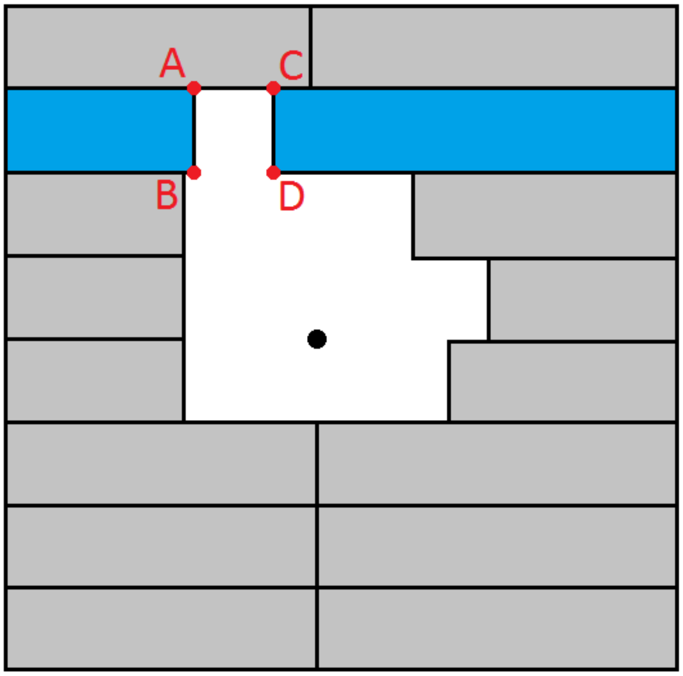

Figure 2.1: An example control point. The leaf pair to be calculated is shown in blue with the corners used labeled A-D.

The points A and B are always the corners of the leaf that is horizontally furthest away from the point of calculation, and points A and C are always the corners that are vertically farthest from the point of calculation. The dimensions of the four rectangular fields are then determined by having a corner at one of the points A through D and their center at the point of calculation. The four fields that would be drawn for the sample control point displayed in Figure 2.1 are shown in Figure 2.2. The fields are labeled A through D based on the points used to draw them.

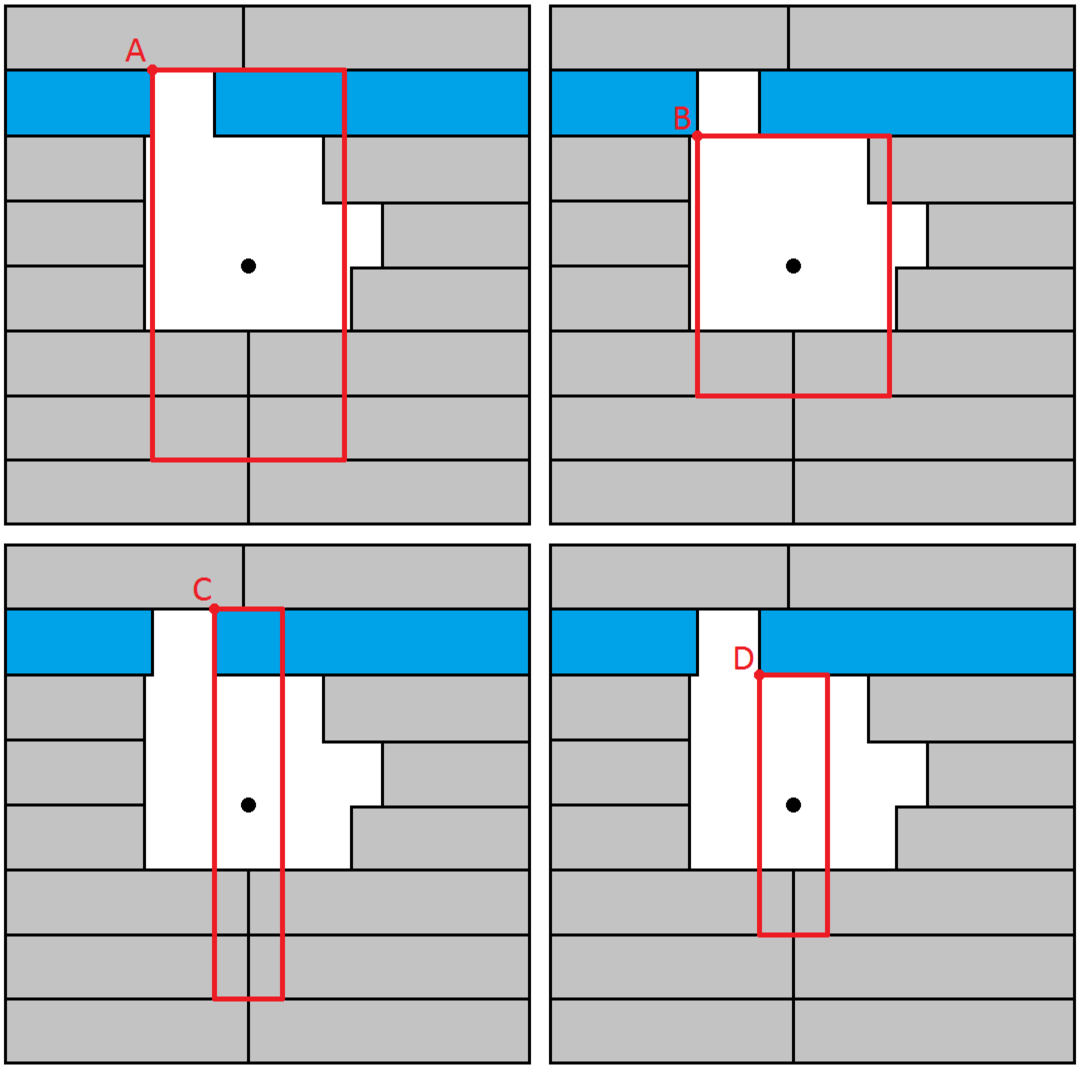

Figure 2.2: Fields A-D. Drawn based on points A-D centered about the point of calculation.

2.1.2 Calculation of Dose per MU of Rectangular Fields

Dose per MU from fields A-D is calculated using the isocentric formalism presented in Task Group 71.[20] A brief summary of the formalism as applied in this project is presented here. For an isocentric photon beam calculation, the dose per MU from a field to a point of calculation is:

$$\frac{D}{MU} = D_o' \cdot S_c(r_c) \cdot S_p(r_d) \cdot TPR\left(d_{eff}, r_d\right) \cdot OAR(d, x) \cdot \left(\frac{SAD}{SPD}\right), \tag{2.1}$$

where:

D: The absorbed dose at the point of calculation.

MU: The number of monitor units for the field.

D'_0: The dose rate or dose per monitor unit of the user's beam under normalization conditions.

d: Depth of the point of calculation.

d_{eff}: Water-equivalent depth of the point of calculation.

OAR: *Off-axis ratio*. The ratio of the open field dose rate at an off-axis point to that of the same field on the central axis at the same depth.

x: *Off-axis distance*. The radial distance from central axis to the point of calculation, measured in a plane perpendicular to the central axis at the isocenter.

r_c: The side of the equivalent square for the collimator field size defined at isocenter.

r_d: The side of the equivalent square for the collimator field size projected to depth d.

S_c: *In-air output ratio*. The ratio of the output (i.e., energy fluence) measured in air for a given field size to that for the reference field size. S_c represents changes in output due to scatter from the flattening filter and photon jaws.

S_p: *Phantom scatter factor*. The ratio of the dose per MU at the normalization depth for a given field size in a water phantom to that of the reference field size for the same incident energy fluence. S_p represents the changes in dose per MU due to the amount of scatter material exposed to primary beam.

SAD: *Source-axis distance*. Distance between the x-ray physical source position and the isocenter.

SPD: *Source-point distance*. The distance from the x-ray physical source to the plane (perpendicular to the central axis) that contains the point of calculation.

SSD: *Source-surface distance*. The distance along the central axis from the physical source to the patient/phantom surface.

TPR: *Tissue phantom ratio*. The ratio of the dose rate at a given depth in phantom to the dose rate at the normalization depth for a given field size.

The rectangular fields A-D are converted to their equivalent squares using the $4 \cdot Area/Perimeter$ approximation.[1] Output factors S_c and S_p, TPRs and OARs are commonly referred to as open field data and are measured at the time of machine commissioning for the purpose of hand monitor unit calculations. The data measured for the Elekta Infinity at Mary Bird Perkins Cancer Center, Baton Rouge, LA (MBPCC) was used. Normalization conditions at MBPCC are a 10x10-cm^2 field size, 10-cm depth and 90-cm source-to-surface (SSD) distance. Additional values for output factors S_c and S_p were measured and calculated as explained in Section 2.2. All data used for input to the algorithm is contained in Appendix B.

2.1.3 Superposition of Fields

Similar to Day's technique for calculating dose to points behind blocked portions of fields,[21] the dose per MU from fields A-D are superimposed in such a manner that the resultant field has the same dimensions as the leaf gap. The superposition depends on the position of the point of calculation relative to the leaf gap. We will continue to illustrate the algorithm using the example control point and leaf gap shown in Figure 2.1. The first step is to take fields of similar width and subtract them from one another. So the dose per MU from field B is subtracted from that from field A, and similarly, field D is subtracted from field C. The results are shown in Figure 2.3. The resultant fields A-B and C-D each have two sections that are the height of an MLC leaf. We then take the dose per MU from field C-D and subtract it from that from field A-B. The resulting dose per MU is that due to the fields shown on the left side of Figure 2.4. The four subfields in the figure all have the same dimensions, with the top left field being the exact size and location of the leaf gap being calculated.

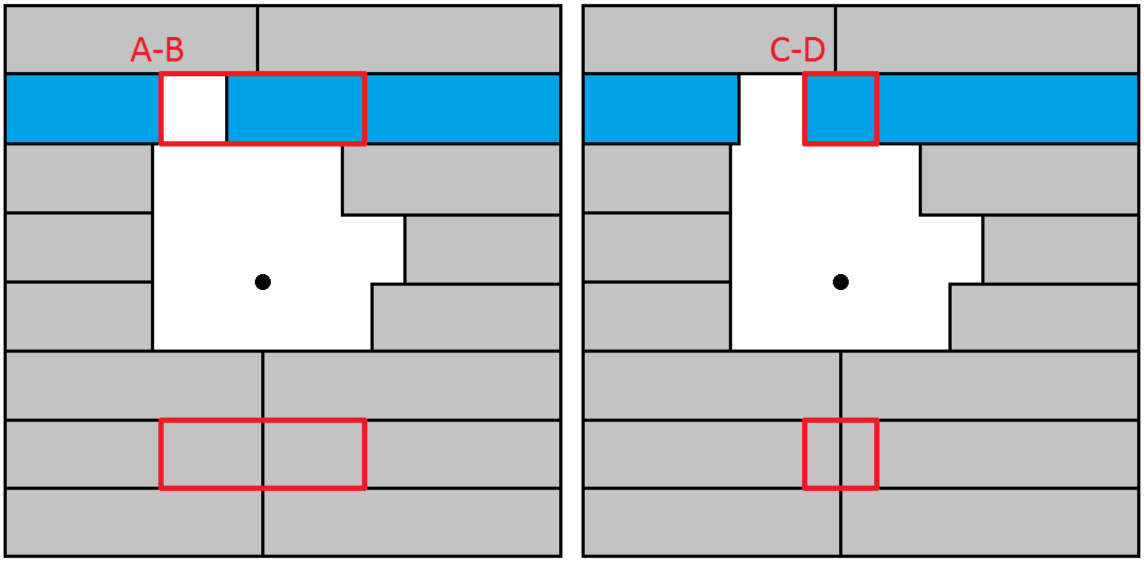

Figure 2.3: First step in the superposition process. On the left is the result of Field A minus Field B. On the right is the result of Field C minus Field D.

Mathematically the dose per MU of these four subfields to the point of calculation would be:

$$D'_{ABCD} = (D'_A - D'_B) - (D'_C - D'_D) \tag{2.2}$$

Where D'_A, D'_B, D'_C, and D'_D are the doses per MU from rectangular fields A, B, C, and D shown in Figure 2.2 to the point of calculation as determined by Equation 2.1. If the point of calculation was on the central axis and assuming scatter is radially symmetric, then each of the subfields pictured on the left of Figure 2.4 should contribute equally to the point. Therefore, we could divide Equation 2.2 by four to determine the dose per MU from the leaf gap to the point of calculation.

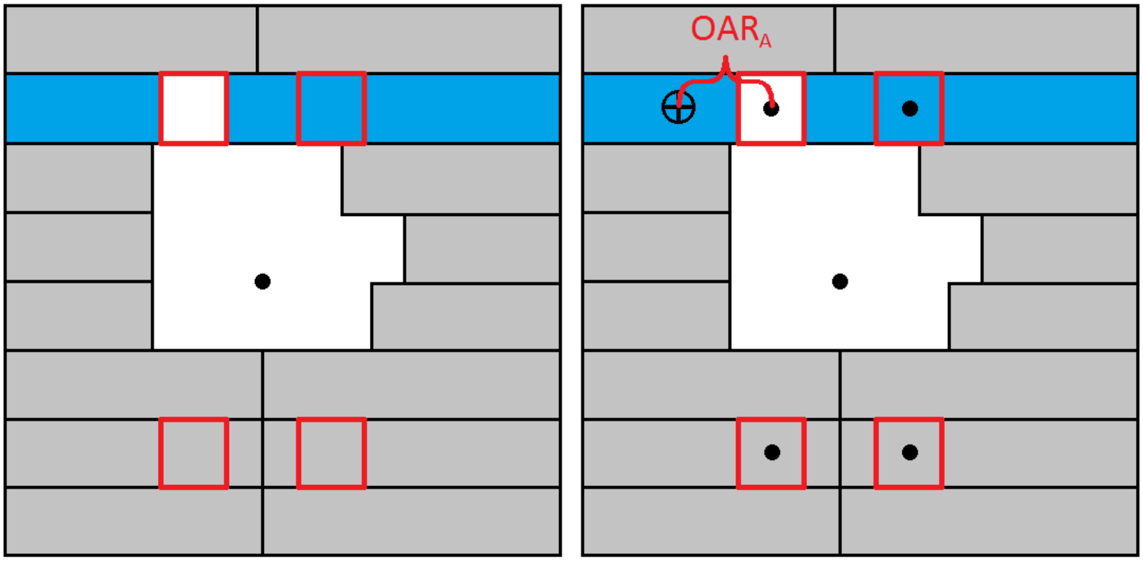

Figure 2.4: Last step in the superposition process. On the left is the result of Field A-B minus Field C-D. On the right an illustration of the distances used to determine OARs for superposition weighting.

Consider the case presented on the right of Figure 2.4, where the point of calculation is off of the central axis, indicated by the black crosshair. The centers of the four subfields are no longer the same radial distance from the central axis and the assumption of radial symmetry is no longer valid. The OAR factor from TG-71 formalism can be used here to determine the correct weighting to give the leaf gap field. The OAR for each subfield is determined based on the distance of the geometric center of the subfield distance from the central axis. The distance used for the leaf gap field is indicated in Figure 2.4 as OAR$_A$. Applying this, the final equation for dose per MU from the leaf gap D$_g$ to the point of calculation is:

$$D'_g = \frac{OAR_A}{OAR_A + OAR_B + OAR_C + OAR_D}\left[(D'_A - D'_B) - (D'_C - D'_D)\right] \qquad (2.3)$$

This expression is valid for the case when the point of calculation is horizontally, and vertically outside of the leaf pair gap. The order of superposition changes based on the position of the point of calculation relative to the leaf gap, other configurations are shown in Appendix A. The general equation for dose per MU from any leaf gap to an arbitrary point of calculation is:

$$D'_g = \frac{OAR_A}{OAR_A + OAR_B + OAR_C + OAR_D}\left[(D'_A \pm D'_B) \mp (D'_C \pm D'_D)\right], \qquad (2.4)$$

where the signs of the $\pm$ and $\mp$ operators depend on the position of the point of calculation relative to the leaf gap.

Since an arbitrary leaf gap can be calculated, the dose per MU from the open area of a control point called D_{open} is simply the sum of all leaf gap doses per MU for each open leaf pair:

$$D'_{open} = \sum_{g}^{Leaf\ Gaps} D'_g. \qquad (2.5)$$

2.1.4 Leakage and Control Point Dose per MU

Leakage dose per MU through the MLC leaves not covered by the collimator is calculated using a single average transmission value α. In this work α is set to a value of 0.4%. This value was measured with a large volume ion chamber with the long axis of the chamber perpendicular to the direction of leaf movement. Readings were taken for a 10x10-cm^2 field defined by the collimating jaws and completely blocked with MLCs. This was divided by the reading of a 10x10-cm^2 defined by both the collimating jaws and MLCs. Figure 2.5 shows all areas used in the leakage calculation for the sample control point from Figure 2.1.

First the dose per MU from the area bounded by the collimating jaws is calculated by the same approach used to calculate the dose per MU from a leaf gap, this is labeled as D_J. Then the dose per MU from the open area of the control point, D_{open}, as calculated by Equation 2.5 is subtracted, giving the dose per MU from the area covered by the MLC leaves. This is multiplied by α to give the leakage dose per MU, D_L, through the MLC leaves for the control point. The mathematical representation is:

$$D'_L = \propto \left(D'_J - D'_{open}\right) \qquad (2.6)$$

This can be combined with Equation 2.5 to give the total dose per MU from a control point to the point of calculation, D_{ctrl}:

$$D'_{ctrl} = \propto \left(D'_J - D'_{open}\right) + D'_{open} \qquad (2.7)$$

Which can be simplified to:

$$D'_{ctrl} = (1-\propto)D'_{open} + \propto D'_J \qquad (2.8)$$

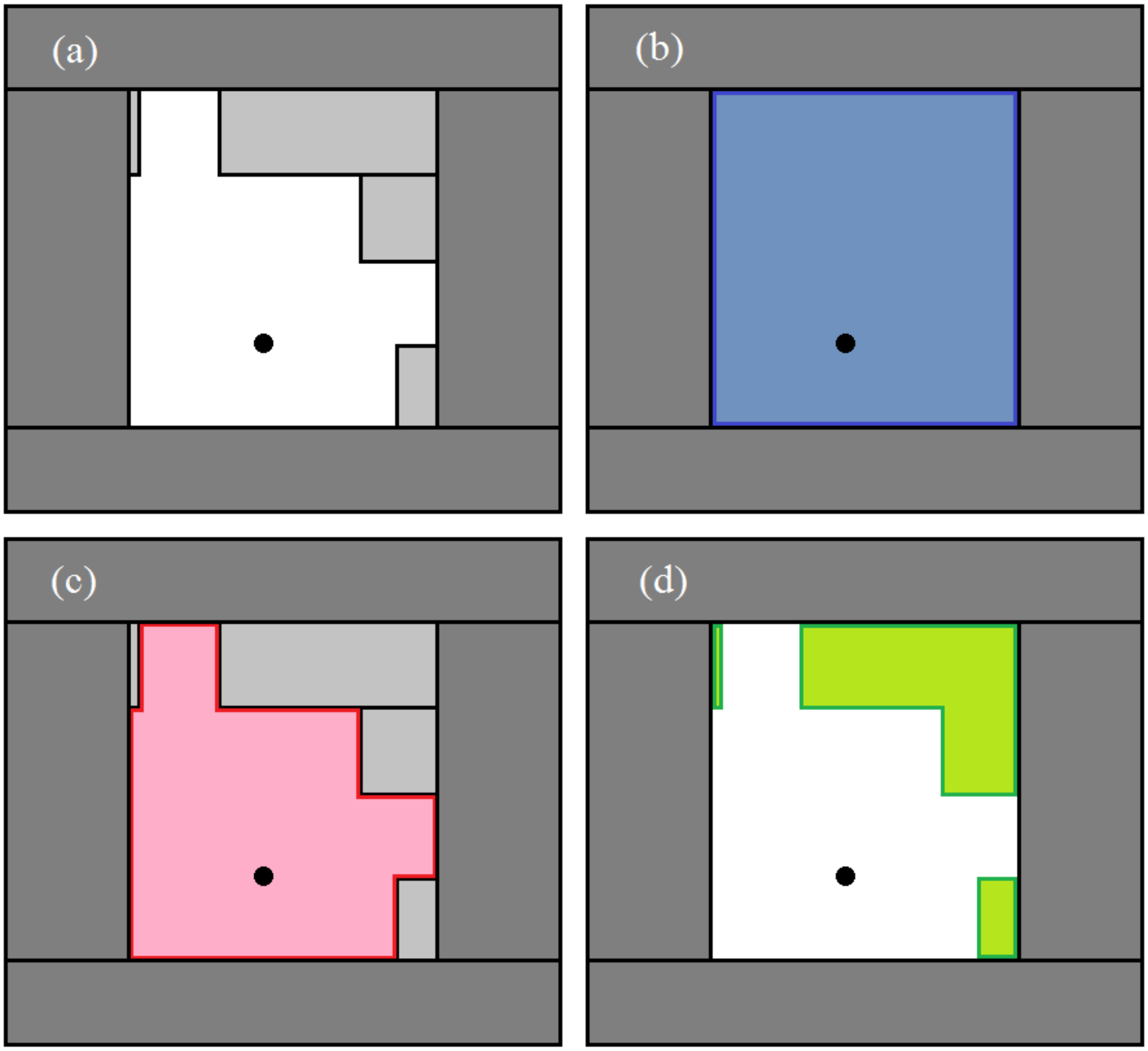

Figure 2.5: Areas used in leakage calculation. (a) Sample control point with the collimator drawn in. (b) The area used to calculate dose per MU D'_J is highlighted in blue. (c) The area contributing dose per MU D'_{open} is highlighted in red. (d) The area that contributes dose per MU D'_L is highlighted in green. Leakage dose through the collimating jaws is ignored in this calculation.

2.1.5 SMLC and VMAT Deliveries

Now that the dose per MU from a control point of an arbitrary MLC configuration can be calculated, doses for SMLC and VMAT deliveries are calculated as the sum of their control point doses with each control point dose per MU multiplied by their respective number of MU:

$$D_{plan} = \sum_{c}^{Control\ Points} MU_c \cdot D'_{ctrl,c} \qquad (2.9)$$

MU_c for the algorithm is the same as used by Pinnacle for their dose calculations as explained in the 2009 SmartArc white paper from Philips.[8]

2.1.6 Program Information

The algorithm was coded in MATLAB® R2010a. Required input information is MLC, collimator, gantry positions, and number of monitor units for each control point as well as the patient coordinates of isocenter and the point of calculation. These values are contained in the DICOM plan file exported from Pinnacle. Depths, water-equivalent or effective depths, and the SSD to the point of calculation are also required and obtained from a custom script created within Pinnacle. Isocenter and point of calculation coordinates are projected to the beam's-eye-view of the control point with appropriate corrections made for beam divergence. Intermediate steps of the algorithm are recorded for debugging purposes, final output is the individual beam and total plan dose. Pinnacle's values for these doses are extracted from the DICOM plan file for direct comparison.

2.1.7 Rectangular Field Testing

Once the algorithm was programmed, several open rectangular fields were calculated and compared to hand calculations to ensure the algorithm was functioning as expected. Fields were calculated on and off the central axis for a range of field sizes, depths, SSDs, and monitor units values. Fields were always symmetric about the point of calculation, which allowed all equivalent squares to be determined mathematically rather than visually. The equivalent square table from BJR supplement #25[22] was used in both the algorithm and hand calculations as the decision to utilize the 4·A/P approximation was made later in the project. This choice of equivalent square algorithm should not affect the results as long as the same method was used by both the algorithm and the hand calculations. The weighting by OAR as shown in Equation 2.3 is also not utilized as it was added later, instead the superposition of the four fields is divided by four.

2.2 Aim 2: Small Field Output Factor Measurements

2.2.1 Output Factors at Small Field Sizes

There are numerous challenges associated with the measurement and calculation of dose of small fields. As such, open field data at Mary Bird Perkins Cancer Center is available down to a field size of 3x3-cm^2. This is sufficient for the majority of clinical applications; however the algorithm can generate fields with equivalent squares much smaller than this during the calculation of leaf gap doses, especially for the leaf pairs adjacent to the point of calculation. TPRs and output factors S_c and S_p are the only open field parameters that are a function of field size. TPRs do not vary significantly with field size, so linear extrapolation is a reasonable approximation of this function below the measured data. Both S_c and S_p are relatively linear at larger field sizes, however there is a rapid drop in values at smaller field sizes, especially for S_p. Since poor estimation of these values is a source of error in the algorithm, S_c and S_p were measured for field sizes smaller than 3x3-cm^2.

2.2.2 Measurement of S_c

The in-air output ratio S_c is measured using an ion chamber in air with enough surrounding buildup material for electronic equilibrium and to prevent electron contamination. Measurements are taken at various field sizes and normalized against a reference field. Task Group 74[23] has been published specifically to deal with measurement of S_c for megavoltage x-ray beams. The methods used here for measurement deviate slightly from the Task Group recommendations for measurement of S_c at small field sizes for reasons explained in later in this section.

A PTW 30006 farmer ion chamber with a sensitive volume of 0.6 cm^3 was used in conjunction with a cylindrical mini-phantom with a 3 cm diameter and 20 cm length designed to fit the chamber. The mini-phantom was aligned with the central axis of the beam at several different source-to-point distances (SPD). This experimental setup put the point of measurement of the ion chamber at a depth of 10 cm, the same as the normalization conditions for the open field data, while providing enough material for lateral electronic equilibrium. The gantry was turned to 270^o and the chamber was placed on the treatment couch held by an acrylic stand to reduce additional scatter in the measurement. A picture of the setup is shown in Figure 2.6.

The point of measurement of the ion chamber was aligned to isocenter using the room lasers and external markings on the mini-phantom. A small piece of film was placed behind the mini-phantom and exposed with the smallest desired field size to ensure the ion chamber was in the center of the field and that the long axis of the chamber was aligned with the central axis. This was an iterative process, with table shifts and rotations of the setup being made based on measurements of the film. A sample film is shown in Figure 2.7.

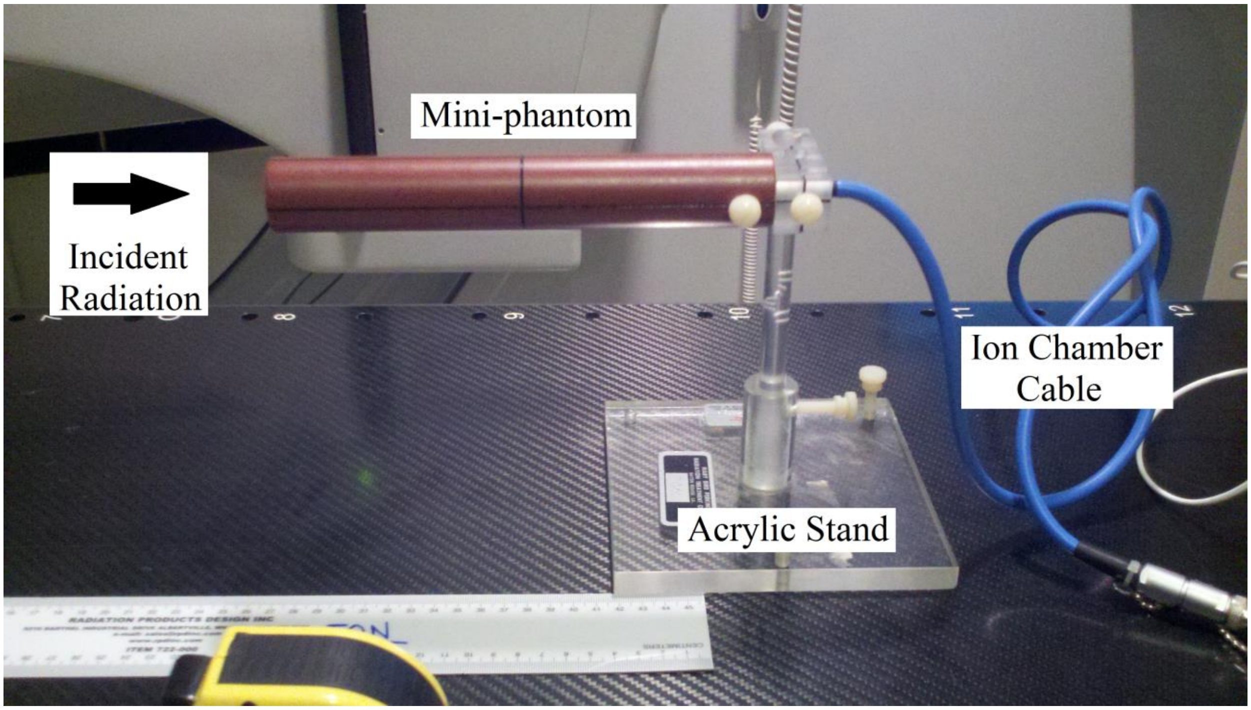

Figure 2.6: The ion chamber and mini-phantom setup used to measure S_c. The center of the sensitive volume of the ion chamber is at the geometric center of the mini-phantom, indicated by the black cross.

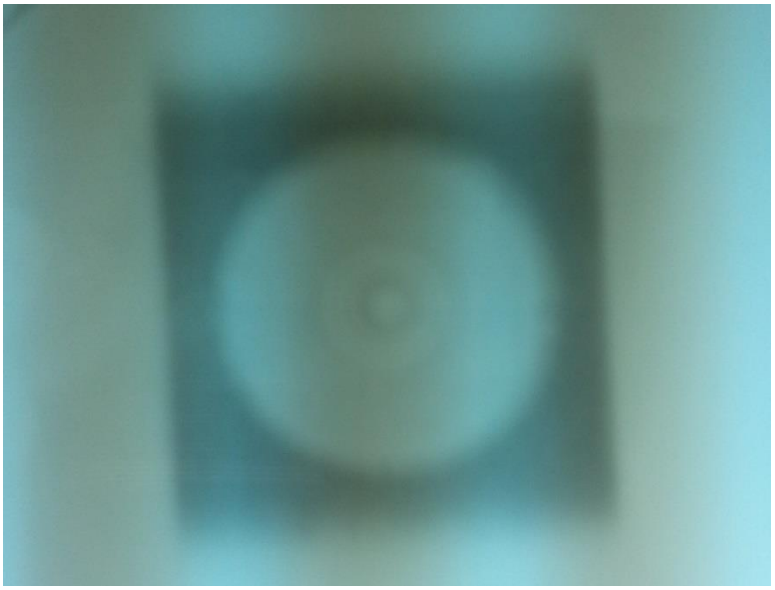

Figure 2.7: Film of a well aligned mini-phantom. There is sufficient and equal flash around all sides of the phantom. Concentricity of circles indicate alignment of the chamber axis with the central axis of the machine.

The mini-phantom was exposed for a set number of monitor units three times per measurement session, for various fields decreasing from the normalization field size. The entire mini-phantom must be contained within the primary beam for each measurement so that in-phantom scatter remains constant. This means, for example, that if the chamber is at isocenter, a 3x3 cm^2 square field is too small to be measured, since the front edge of the phantomwould be clipped as the field size at 90 cm from the source is 2.7x2.7-cm^2. Since fields smaller than 3x3-cm^2 are desired, the chamber is placed at extended distance. Field divergence allows for the measurement of smaller fields, while providing sufficient flash around the phantom. However this gives rise to certain effects that must be taken into account.

At small field sizes, changes in output in-air are primarily due to the direct source-obscuring effect. While the primary x-ray source is always visible, the scattered photon source (sometimes called the extrafocal source), which primarily originates from the flattening filter, can become obscured by the collimator jaws, which results in a substantial reduction in output.[23] From the view of the point of measurement of the ion chamber looking back at the treatment head (point's-eye-view or PEV), the visible amount of extrafocal source changes as a function of SPD. As the point of measurement moves farther from the treatment head, the amount of flattening filter visible deceases for the same nominal collimator setting, as shown in Figure 2.8. Therefore, if measurements were taken at extended SPD and normalized to a nominal 10x10-cm^2 field, the resultant S_c values would be different.

To account for this, a correction based on work done by Lam and Haken[24] is used. For each measurement at extended SPD, the size of the field from the PEV as defined by the upper edges of the collimators projected to the plane of the flattening filter is:

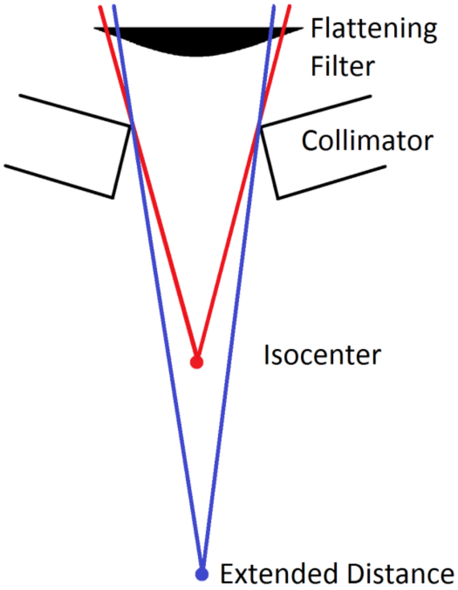

Figure 2.8: An illustration of the change in visible flattening filter from the PEV, as limited by the top of divergent collimator jaws, as a function of SPD in the measurement of S_c. Measurements at isocenter (red) have a larger view of the extrafocal source of scatter than those at extended distances (blue).

$$r_{ff} = r_n \cdot \frac{SCD}{SAD} \cdot \frac{SPD - SFD}{SPD - SCD}, \tag{2.10}$$

where:

r_{ff}: The size collimator opening for the photon jaw being projected in the PEV to the plane of the flattening filter.

r_n: The nominal collimator setting for the jaw being projected. Defined in the plane of isocenter.

SCD: *Source-collimator distance*. The distance from the physical x-ray source to the top of the jaw being projected.

SFD: *Source-flattening filter distance*. The distance from the physical x-ray source to the bottom of the flattening filter.

Other terms in the equation were defined in Section 2.1.2. The calculation of r_{ff} is performed individually for the X and Y sizes, since they correspond to the upper and lower photon jaws, each of which has a different SCD. Once the collimator size has been projected to the plane of the flattening filter in the PEV, Equation 2.10 can be modified to solve for the nominal jaw setting that gives the same PEV field size at the flattening filter:

$$r_{iso} = r_{ff} \cdot \frac{SAD}{SCD} \cdot \frac{SAD - SCD}{SAD - SFD} \tag{2.11}$$

Where r_{iso} is the field size at isocenter that has the same PEV field size as the point at extended SPD. S_c values are graphed as a function of r_{iso} instead of r_n, correcting for changes in the amount of effective x-ray source visible as a function of SPD.

Output factors were measured at SPDs of 1-m, 2-m and 3.07-m. Nominal field sizes r_n were chosen to give a desired r_{iso}. The largest r_{iso} for each SPD was set to a 10x10-cm^2 field. This allowed for easy aggregation of the data from different SPDs. Multiple ion chamber readings were taken for each field size and averaged. S_c values were normalized to a r_{iso} of 10x10-cm^2. SCDs of the top and bottom collimators were 29.5-cm and 43.1-cm respectively and the SFD was 15.9-cm. Values were obtained from of the MLCi2 geometry in the Elekta User Manual. Data was taken in two different sessions and averaged together for the final values.

2.2.3 Determination of S_p

The phantom scatter factor S_p was determined indirectly from the in-water output ratio S_{cp}, and S_c. S_{cp} is measured using an ion chamber placed in scattering material while changing the field size. Measurements are normalized against a reference field size. An Exradin A16 chamber was used with a sensitive volume of 0.007-cm^3. It was placed in solid water with a chamber specific cavity at 90-cm SSD, 10-cm depth, with 11-cm of back scatter material. The gantry was set to 0^o and the chamber was roughly aligned to the central axis using the light field crosshair and external markings on the solid water slab.

To ensure that the chamber was centered within the small fields, the chamber position was adjusted until the signal was maximized. The collimators were set to the smallest field size and measurements were taken while first shifting the couch laterally in 0.1-cm increments looking for the point of maximum signal. The superior/inferior direction was then searched in a similar manner placing the chamber in the center of the smallest field size.

Once the chamber was centered, measurements were taken at various field sizes ranging from 1x1 to 10x10-cm^2. Megavoltage portal images of the setup using the EPID were taken at each field size, imported into RIT113 v6.0 where the full width at half maximum (FWHM) of the radiation across perpendicular directions of the field was determined. Data for a nominal collimator setting of 1-cm was dropped as the EPID data was saturated in the center of the field, giving an inaccurate FWHM. FWHM field sizes and ion chamber readings from two measurement sessions were averaged together. A three point quadratic interpolation was then used to change S_{cp} from FWHM field sizes to desired field sizes that aligned with r_{iso} values for the S_c measurements.

After S_c, and S_{cp} were successfully measured, data existed for both at field sizes of 1.5, 1.67, 2, 2.5, 3, 4, 5, 7.5, and 10x10-cm^2. S_{cp} values were then divided by S_c to determine S_p. Percent errors against data book values were calculated for S_c and S_p using the equation:

$$\%\,Error = \left(\frac{Measured}{Known} - 1\right) \cdot 100. \qquad (2.12)$$

2.2.4 Exponential Fits of Output Factors

A field size of 1.5x1.5-cm^2 is the smallest size we could measure with reasonable certainty. However the algorithm may require calculation of rectangular fields whose equivalent squares are smaller than this, so accurate extrapolation of output factors was required. In this project we assumed the output reaches a value of zero at zero field size and output factors below measured data follow an exponential function in the form of:

$$OF(r) = a(1 - e^{-b \cdot r}) \qquad (2.13)$$

Where a and b are fitting parameters, and r is the field size. Since output factors are relatively flat with a fall off at smaller field sizes, a limited number of points were used when fitting instead of the entire curve. The three smallest field sizes were used for each curve and the fit was verified to give good agreement at the smallest measured field size. Fit values for output factors were only used for field sizes below measured data.

2.3 Aim 3: Compare the Algorithm Against Pinnacle and Ion Chamber Measurements of AAPM Report Task Group 119 Cases

2.3.1 Summary of AAPM Report Task Group 119

The report from AAPM Task Group 119: IMRT commissioning[19] outlines an approach as well as standards for commissioning a clinic's IMRT planning and delivery systems. They presented multiple sets of contours that are placed on a dosimetry phantom within the treatment planning system. The geometries are representative of sites commonly treated with IMRT. Dose goals for each site as well as beam arrangements were specified. Plans are delivered on a dosimetry phantom and measured at various recommended points with an ion chamber. The report specifies a confidence limit or interval of acceptable differences between planned and measured values.

Mancuso et al. planned, delivered, and measured the TG-119 cases using both VMAT and SMLC-IMRT deliveries at our institution.[25, 26] Using the algorithm to independently calculate doses from these plans would indicate the algorithm performance for representative IMRT geometries and allow for comparison against dose measurements as well as values calculated by Pinnacle.

2.3.2 Commissioning Process Performed by Mancuso et al.

Four of the TG-119 geometries were investigated, the multitarget, mock prostate, mock neck, and C-shape. Cross-sectional slices of the structure set of each case as are available for download at http://www.aapm.org/pubs/tg119/default.asp and shown in Figure 2.9. For each geometry, TG-119 supplies DVH dose goals for each structure, (Table 2.1) the beam configuration for an SMLC delivery to be used, as well as points of comparison for measurement.

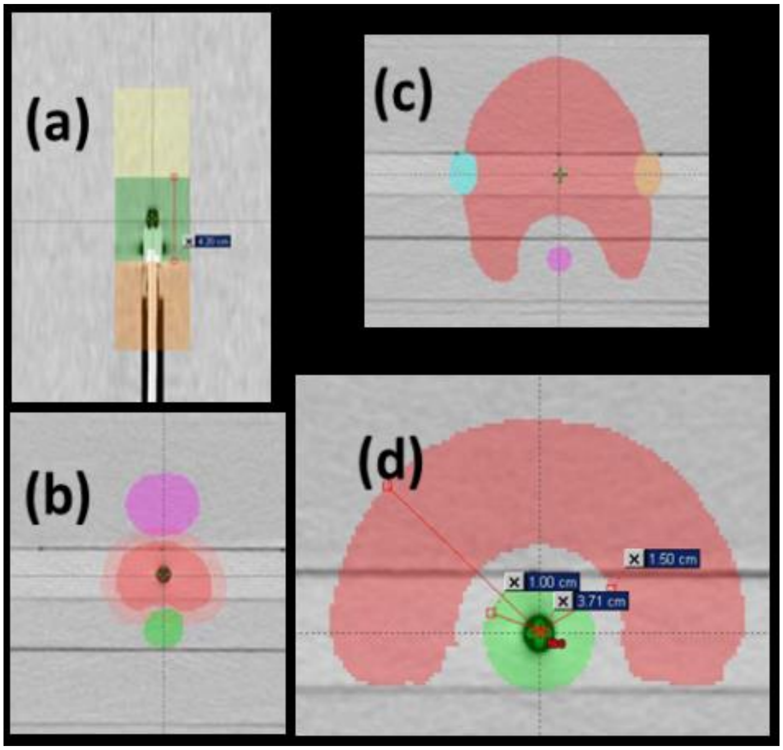

Figure 2.9: Cross sectional slices of the TG-119 test geometries. (a) Multitarget, (b) mock prostate, (c) mock neck, and (d) C-shape geometries. From Mancuso et al.[26]

TG-119 structure sets were copied onto a cylindrical cheese phantom and planned according to the report's protocols. In addition to the SMLC plans outlined in the report, VMAT plans for each site of one to two arcs that met the same dose goals were created. Plans were delivered to the phantom and ion chamber measurements were taken at points specified by the report. Ion chamber measurements were taken five times for each point and a mean dose was determined. Ion chamber calibration followed the recommendations of TG-119. A 10x10-cm^2 parallel opposed AP-PA plan was created in Pinnacle. The ion chamber was placed closest to the center of the phantom and prescribed 200 cGy. The plan was delivered and a ratio of cGy to electrometer reading was determined. Dose was also determined using the calibrated $N_{D,w}$ of the chamber, the P_{elec} of the electrometer, and using temperature and pressure corrections to the ion chamber readings. Calibration methods calculated dose values within 0.6% for all measurement sessions.[26] Measurements were also taken in the coronal and sagittal planes with a commercial 2D diode array and radiochromic film. In this work, comparisons were only made against the point ion chamber measurements.

Table 2.1: Dose goals for the TG-119 geometries. Adapted from TG-119.[19]

Planning parameter	Plan goal (cGy)	Planning parameter	Plan goal (cGy)
Multitarget		**Prostate**	
Central target D99	> 5000	Prostate D95	> 7560
Central target D10	< 5300	Prostate D5	< 8300
Superior target D99	> 2500	Rectum D30	< 7000
Superior target D10	< 3500	Rectum D10	< 7500
Inferior target D99	> 1250	Bladder D30	< 7000
Inferior target D10	< 2500	Bladder D10	< 7500
Neck		**C-shape**	
PTV D90	5000	PTV D95	5000
PTV D99	> 4650	PTV D10	< 5500
PTV D20	< 5500	Core D10	< 2500
Cord maximum	< 4000		
Parotid D50	< 2000		

For this work, Pinnacle[3] back-ups of the plans were restored and the data necessary to run the algorithm were extracted. Each point with an ion chamber measurement was calculated for comparison by MuCheck version 8.2 and the algorithm as explained in Sections 2.4.5 and 2.4.6 respectively.

2.3.3 Test Case Geometry Description

The multitarget geometry consists of three cylindrical targets stacked along the axis of rotation, with the center of the middle target at isocenter. Each target has a different dose goal, the middle being the highest at 50 Gy. The superior target receives 50% and the inferior 25% of the middle target's goal. Seven fields at 50^o gantry intervals from the vertical with 6 MV energy were used in planning. Ion chamber measurements were made at center of each target.

The mock prostate contains a central planning target volume (PTV) that overlaps with the rectum and bladder. Seven fields at 50^o gantry intervals from the vertical with 6 MV energy were used. Ion chamber measurements were made in the center of the PTV at the isocenter, as well as in the center of the rectum and bladder.

The mock neck has a central PTV with critical structures being lateral parotids and a posterior spinal cord. Nine fields at 40^o gantry intervals from the vertical with 6 MV energy were used. Ion chamber measurements were made in the center of the PTV at isocenter and at the center of the spinal cord.

The C-shape geometry consists of a curved target surrounding a cylindrical critical structure centered at isocenter. Nine fields at 40^o gantry intervals from the vertical with 6 MV energy were used. Ion chamber measurements were made at isocenter and in the center of the PTV, which was located directly anterior to isocenter. There were two sets of prescribed dose goals for the C-shape, the easier one being used in this work.

2.4 Aim 4: Compare the Algorithm Against Pinnacle for Patient Plans

2.4.1 Overview

In order to evaluate clinical performance of the algorithm, a series of clinical plans of patient geometries were calculated. Three sites were chosen for investigation, the prostate, neck, and chest wall. For each site, five patients with VMAT plans were found and placed in a HIPAA-compliant database. For each of the patient datasets, SMLC plans were created using the same dose goals as the VMAT plans. This gives five plans per modality per site, for a total of thirty patient plans. Dose was evaluated at one point for each plan selected as explained in Section 2.4.4. Pinnacle dose was compared against results from calculations using MuCheck v8.2 and the algorithm as explained in Sections 2.4.5 and 2.4.6 respectively.

2.4.2 Selection of Sites

These sites were chosen as they are common places for IMRT delivery and each has unique calculation challenges. The prostate has few heterogeneities, relatively simple geometry, and the point of calculation is at isocenter. The head and neck has multiple small heterogeneities such as airways, the spinal cord, and jaw bones. It is geometrically complex with critical structures adjacent to or in target volumes, with a point of calculation near the isocenter. The chest wall has large tissue air interfaces due to the proximity to the lung and is a curving target that covers a large volume. The point of calculation is far from isocenter, which is usually placed in the lung.

2.4.3 Plan Selection and Creation

Five patients were found for each site that had VMAT plans consisting of one or two arcs. Each plan had been previously approved for treatment by a physician. SMLC plans were created with the goal of matching the DVH and coverage of the original VMAT plans. For the prostate and neck sites, nine beams at 40^o intervals from the vertical were used. For the chest wall, beams were placed at 30^o intervals across the span of the VMAT arc, resulting in seven to eight beams per plan. All plans were calculated using Pinnacle version 9.2. The standard Mary

Bird Perkins Cancer Center optimization protocol for SMLC planning was used. The optimization parameters are listed in Table 2.2.

Table 2.2: DMPO optimization parameters used for SMLC plans.

DMPO Optimization Parameters	Value
Max Iterations	40
Convolution dose iteration	16
Stopping tolerance	1e-05
Apply tumor overlap function	No
Allow jaw motion	Yes
Use current jaws as max	No
Split if necessary	No
Maximum number of segments	10 times the number of beams
Minimum segment area	4
Minimum segment MUs	4
Minimum number of leaf pairs	4
Minimum leaf end separation	4
Minimum overlap distance	2
Maximum overlap distance	4
Compute final dose	Yes
Use SVD for dose calculation	No

The optimization was terminated when the DVHs of the SMLC plans were found to be equal to the results from the corresponding VMAT plan. At least one SMLC plan of each site was reviewed by a dosimetrist and determined to be sufficiently matched and clinically acceptable.

2.4.4 Selection of Calculation Point

The appropriate selection of a point of calculation for a second check is vital in achieving an accurate verification. Areas of electronic disequilibrium should be avoided, such as found in high-gradient regions, near tissue interfaces, and within 2 cm of field edges.[5] Unfortunately, since IMRT treatments are made of the sum of multiple smaller fields, it is impossible to avoid field edges of all subfields when choosing a calculation point.

Calculation points for the VMAT plans were chosen during the initial planning by a dosimetrist. The point was manually placed on the slice with the largest area of the PTV in the center of the PTV contour on that slice. This was generally a high dose, low gradient region in homogeneous tissue. For this project those were the points used for the calculation of plans unless they were within 1 cm of a tissue interface. In this case it was moved on the same slice until it was 1 cm away from the interface. One point was used for comparison for each patient for the SMLC and VMAT plans.

2.4.5 MuCheck Calculations

Secondary calculations of IMRT plans at Mary Bird Perkins Cancer Center are currently performed using MuCheck version 8.2. All points calculated by the algorithm are also calculated using this software as it is useful to be able to compare against the current standard of care. Off-axis VMAT points are excluded from all statistical analysis as they are not intended for calculation by the version of MuCheck used in this work for two reasons.

The first being that only average values for SSDs, depths, and effective depths are used in the calculation. This is a reasonable approximation if there is not a large variation in depth over the range of the VMAT arc, such as for prostate plans, where the point of calculation is in the center of a homogeneous area of the patient. For chest wall treatments, this is less valid as the isocenter is usually placed in the lung with the point of calculation in the chest wall itself.

The second reason MuCheck fails for these calculations is that the current version does not account for changes in off-axis position as a function of gantry angle. Thus, for each VMAT control point, MuCheck places the calculation point at the same location within the beams eye view projection for all gantry angles. This is incorrect for all points outside of the isocenter. Since MLC patterns for VMAT deliveries are generally a thin opening that sweeps from one side of the field to another, this means that the point of calculation can be erroneously placed outside the field for a majority of the control points being calculated.

MuCheck requires pinnacle-exported DICOM files with SSDs, geometric depths, and effective depths to the point of calculation being manually input. Isocenter and point of calculation DICOM coordinates are also required for projection of the point of calculation into the beam's-eye-view.

2.4.6 Algorithm Calculations

The point of calculation is created as a point of interest within Pinnacle and selected as the reference point for monitor unit calculations. This ensures that the correct point coordinates are contained in the exported DICOM file. The RT plan is exported using the DICOM export functionality contained within Pinnacle. A custom script is then executed that writes SSDs, depths, and effective depths to the point of calculation to a text file. This text file, along with the RTPLAN DICOM file, contain all necessary plan information for algorithm calculations.

Open field data is contained in comma separated value spreadsheets that are read by the algorithm at time of execution. All algorithm calculations in this project were done with additional measured small field output factors, as explained in Section 2.2, and with exponential fits of output factors for small field sizes as explained in Section 2.2.4.

Chapter 3 : Results and Discussion

3.1 Rectangular Field Calculations

The results of the rectangular fields along with their parameters needed for hand calculations are listed in Table 3.1 and Table 3.2 for the on- and off-axis calculations, respectively.

Table 3.1: Parameters and results of rectangular fields calculated on the central axis.

Central Axis Calculations							
Field Number	1	2	3	4	5	6	7
X Field Size (cm)	10	10	19	7	5.75	3.25	10.75
Y Field Size (cm)	10	10	7	19	10.25	35.75	20.25
Depth (cm)	10	10	10	10	2	12.2	23.75
SSD (cm)	90	90	90	90	80	99.8	109.3
Monitor Units	100	150	100	100	100	100	100
Algorithm Dose (cGy)	80	120	80	80	145.8	54.3	30.4
Hand Calculation Dose (cGy)	80	120	80	80	145.8	54.3	30.4

Table 3.2: Parameters and results of rectangular fields calculated off the central axis.

Off Axis Calculations								
Field Number	8	9	10	11	12	13	14	15
Point of Calculation (x,y)	2, 2	5, -5	-12, 8	9, -15	5.3, -6	5.3, -6	-6, 5.3	-6, 5.3
X Field Size (cm)	10	10	13	14	10.2	14.75	10.2	14.75
Y Field Size (cm)	10	10	18	8	14.75	10.2	14.75	10.2
Depth (cm)	10	10	10	2.5	7.2	7.2	7.2	7.2
SSD (cm)	90	90	90	85	97.7	97.7	97.7	97.7
Monitor Units	100	100	100	100	100	100	100	100
Algorithm Dose (cGy)	81.0	81.3	85.2	134.4	83.8	83.8	83.8	83.8
Hand Calculation Dose (cGy)	81.0	81.3	85.2	134.4	83.8	83.8	83.8	83.8

All fields show exact agreement between the algorithm and hand calculations. This is expected as both methods use the same input data and make the same assumptions. This demonstrates that field data are being correctly read and interpolated by the algorithm and equivalent squares are being correctly determined.

3.2 Output Factors

Data table and measured output factors are shown in Table 3.3. As explained in Section 2.2.3, S_p was not directly measured; rather it was found by dividing S_{cp} by S_c. Percent errors between measured and data table values are well within 1% for all cases. Values for the fitting parameters in Equation 2.13 for all fits are displayed in Table 3.4.

Table 3.3: Results of output factor measurements. Compared against data table values.

Field Size (Side of the Equivalent Square) [cm]	Measured Values			Data Table Values		
	S_c	S_p	S_{cp}	S_c	S_p	S_{cp}
10	1	1	1	1	1	1
7.5	0.988	0.966	0.955			
5	0.975	0.922	0.900	0.973	0.927	0.903
4	0.968	0.906	0.876			
3	0.957	0.880	0.842	0.954	0.884	0.843
2.5	0.955	0.863	0.823			
2	0.950	0.834	0.793			
1.67	0.947	0.806	0.763			
1.5	0.941	0.768	0.722			

Table 3.4: Exponential fitting parameters for output factors. Variables are listed for Equation 2.13.

Fitting Parameter	Measured	
	S_c	S_p
a	0.953	0.909
b	2.938	1.263

Figure 3.1 and Figure 3.2 are graphs of the measured values and their fits for S_c and S_p respectively. The data used in the exponential fit are denoted by a solid line through the measured points while extrapolated data are shown by a dashed line. Fit values were only used by the algorithm below a field size of 1.5x1.5-cm^2. Both fits display a smooth transition from data to the fit.

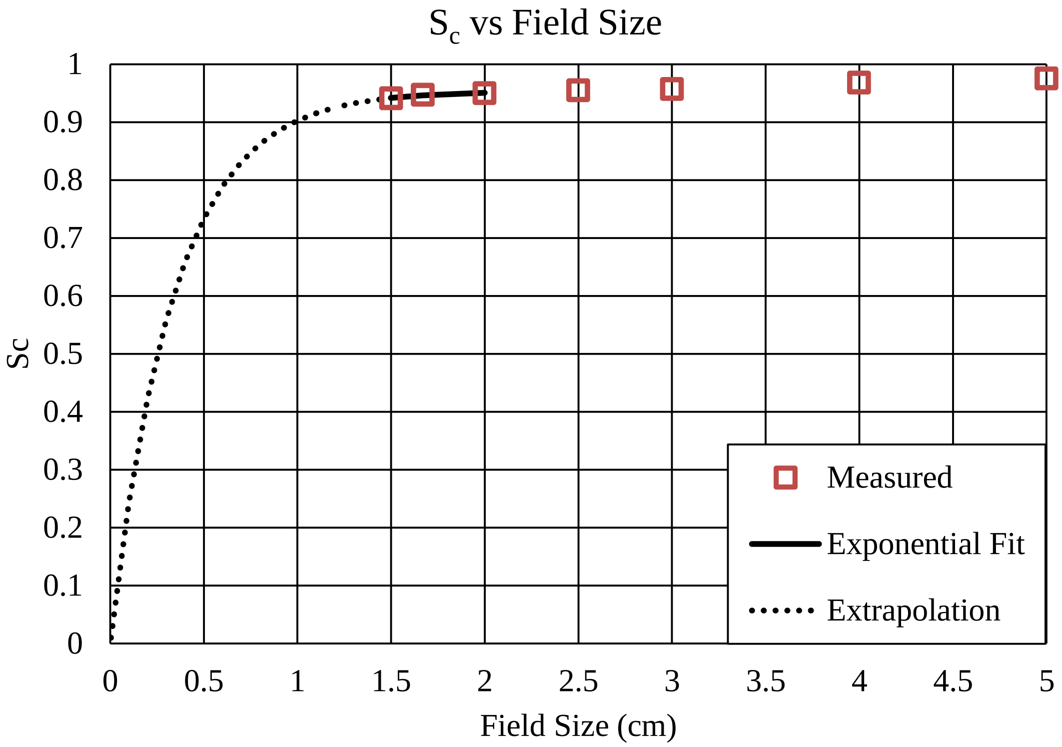

Figure 3.1: Graph of S_c versus field size.

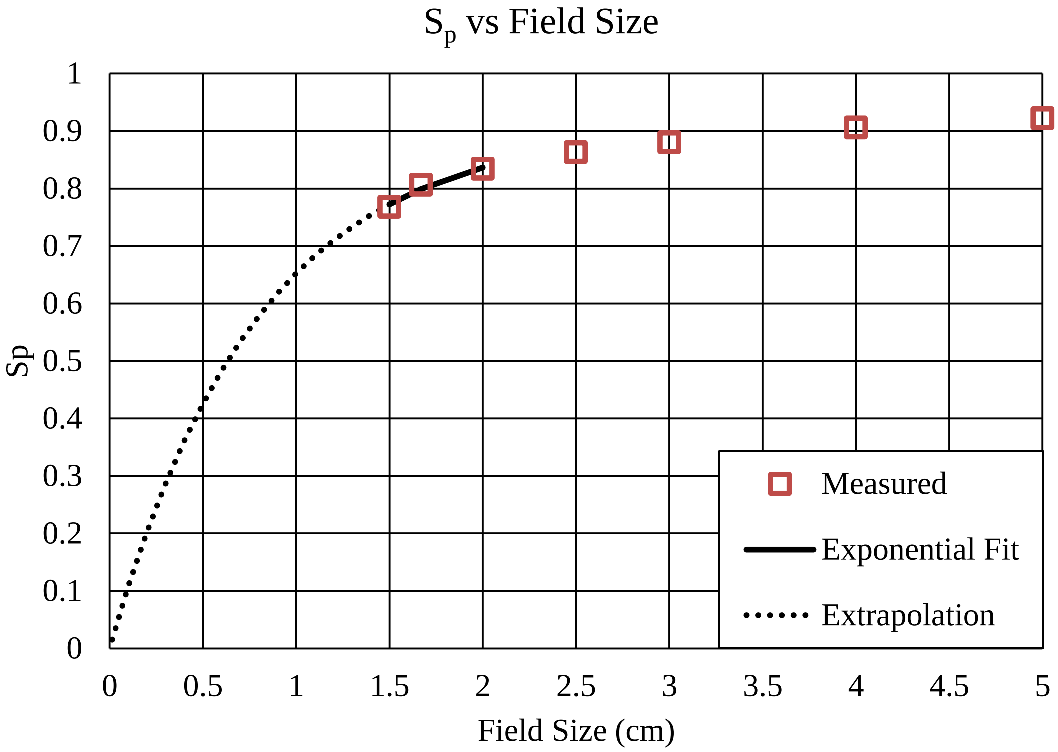

Figure 3.2: Graph of S_p versus field size.

3.3 TG-119 Test Cases

For each test case, each point with an ion chamber measurement (listed in Section 2.3.3) was calculated by Pinnacle version 9.0, MuCheck version 8.2, and the algorithm. Percent errors against the ion chamber measurements and Pinnacle-calculated point doses were determined for both the MuCheck and algorithm calculations using Equation 2.12. None of the ion chamber measurements were made at isocenter, so for reasons explained in Section 2.4.5, no VMAT plans were calculated by MuCheck for this aim. Additionally, MuCheck was not able to calculate two points, the PTV in the C-shape geometry and the bladder in the mock prostate. The error given was that a point was outside of the field for a beam in the plan.

Mean values for algorithm calculations are higher than desired. The percentage of plans that have errors of 2% or less were 55% (11 of 20) and 65% (13 of 20) when compared against Pinnacle and ion chamber measurements respectively. This is significantly lowered than desired. Since all available points were used when determining these results, some points do not meet the criteria listed in Section 2.4.4 for acceptable points for a secondary calculations. Excluding points that do not meet the criteria leaves only the PTV for calculation for each geometry.

Table 3.5 shows mean percent errors with standard deviations for all plans grouped by calculation method and modality as compared against Pinnacle doses and ion chamber measurements. Full results are contained in Appendix C. As compared to MuCheck, the algorithm had equivalent mean errors but with noticably smaller standard deviations. These indicate that the algorithm had more precise calculations than MuCheck.

Mean values for algorithm calculations are higher than desired. The percentage of plans that have errors of 2% or less were 55% (11 of 20) and 65% (13 of 20) when compared against Pinnacle and ion chamber measurements respectively. This is significantly lowered than desired.

Since all available points were used when determining these results, some points do not meet the criteria listed in Section 2.4.4 for acceptable points for a secondary calculations. Excluding points that do not meet the criteria leaves only the PTV for calculation for each geometry.

Table 3.5: Results of all TG-119 calculation points. Mean percent errors and standard deviations aggregated by calculation method.

Calculation Method	**Pinnacle % Error**	**Measurement % Error**
All Plans	**Mean ± Std. Dev. [%]**	**Mean ± Std. Dev. [%]**
MuCheck	-3.2 ± 12.5	-1.4 ± 10.3
Algorithm	-3.9 ± 3.7	-1.7 ± 2.8
SMLC		
MuCheck	-3.2 ± 12.5	-1.4 ± 10.3
Algorithm	-3.3 ± 2.8	-1.7 ± 3.0
VMAT		
MuCheck	N/A	N/A
Algorithm	-4.5 ± 4.5	-1.7 ± 2.8

Table 3.6 shows mean percent errors with standard deviations for all plans for only acceptable calculation points. When compared against Pinnacle doses, there is little difference observed between MuCheck and algorithm calculations. When compared against ion chamber measurements mean values are equivalent for both methods, while MuCheck has significantly lower standard deviations. The percentage of plans that have errors of 2% or less were 88% (7 of 8) and 88% (7 of 8) when compared against Pinnacle and ion chamber measurements respectively. All metrics show improvement once unacceptable points of calculation are excluded, indicating that performance of both algorithms improve when the point is in a high dose, low gradient region. Excluding unacceptable points greatly reduces statistics of the points weakening any further conclusions.

Table 3.6: Results of acceptable TG-119 calculation points. An acceptable point meets the criteria outlined in Section 2.4.4.

Calculation Method	Pinnacle % Error	Measurement % Error
All Plans	**Mean ± Std. Dev. [%]**	**Mean ± Std. Dev. [%]**
MuCheck	-2.1 ± 1.3	-0.8 ± 0.1
Algorithm	-1.5 ± 1.1	-0.4 ± 1.4
SMLC		
MuCheck	-2.1 ± 1.3	-0.8 ± 0.1
Algorithm	-1.5 ± 0.4	-1.0 ± 1.8
VMAT		
MuCheck	N/A	N/A
Algorithm	-1.6 ± 1.5	0.2 ± 0.9

3.4 Patient Plans

The algorithm was used to calculate a point dose for SMLC and VMAT plans of 15 patients evenly divided between the prostate, neck, and chest wall as explained in Section 2.4. Percent error values for each plan were calculated using Equation 2.12 with the Pinnacle dose as the known value. A table with the results of all plans is included in Appendix D.

Table 3.7 shows mean percent errors and 95% confidence intervals for each calculation method as a function of modality. Algorithm calculations show lower average errors and 95% confidence intervals than MuCheck calculations with the most significant improvement being to the confidence intervals. While there is some slight difference in SMLC and VMAT plans for algorithm calculations, it is not appreciable. Little to no difference is expected as the calculation method is the same and monitor units are assigned to control points in the same manner as Pinnacle.

Figure 3.3 and Figure 3.4 are histograms of percent errors for MuCheck and algorithm calculations respectively with different anatomical sites noted. MuCheck exhibits a wide range of errors with no apparent correlation as a function of site. Algorithm calculations are spread over a much smaller interval. Systematic offsets are apparent for each site, prostate doses being underestimated and chest wall doses being overestimated. Neck calculations are well centered near zero.

Table 3.7: Results of patient plan calculations aggregated by modality.

All Sites	**MuCheck % Error Mean ± 95% Conf. Int. [%]**	**Algorithm % Error Mean ± 95% Conf. Int. [%]**
Both	0.7 ± 7.2	-0.2 ± 3.8
SMLC	0.8 ± 7.3	0.2 ± 4.1
VMAT	0.3 ± 7.5	-0.6 ± 3.4

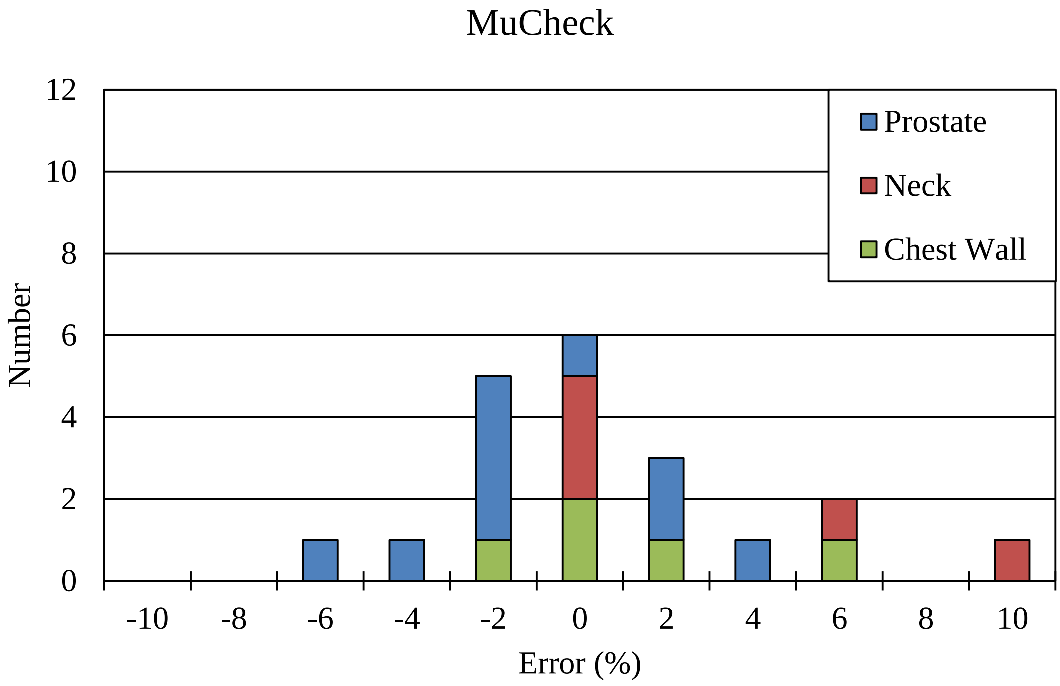

Figure 3.3: Histogram of percent errors for MuCheck calculations.

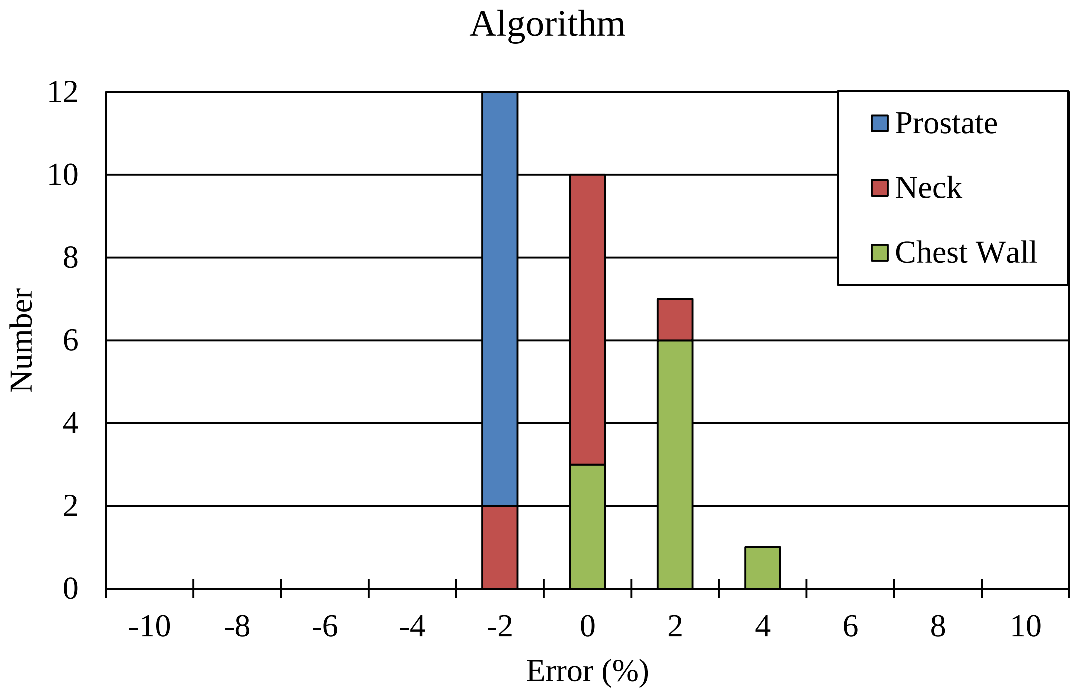

Figure 3.4: Histogram of percent errors for algorithm calculations.

Table 3.8 shows the mean percent errors and the 95% confidence interval grouped by site for each calculation method. The mean error for algorithm calculations of the prostate is greater than MuCheck, lower for neck calculations, and roughly equivalent for chest wall calculations. Systematic offsets are apparent with roughly a 2% underestimate and overestimate of dose for the prostate and chest wall, respectively. Reasons for this are presented later in this section. Confidence intervals show improvement in all cases indicating a more precise calculation than MuCheck.

The TG-71 dose calculation formalism is a dose calculation model that is based on a few assumptions, deviation from which is the source of these observed errors. One assumption is that the field being calculated is square, as data tables are built using measurements of square fields. Rectangular field approximations allow for the calculation of various field sizes and the

Table 3.8: Results of patient plan calculations aggregated by treatment site.

Site	**MuCheck % Error Mean ± 95% Conf. Int. [%]**	**Algorithm % Error Mean ± 95% Conf. Int. [%]**
All Sites	0.7 ± 7.2	-0.2 ± 3.8
Prostate	-1.0 ± 5.8	-2.1 ± 0.9
Neck	3.3 ± 8.8	-0.3 ± 2.4
Chest Wall	1.6 ± 5.1	1.8 ± 2.5

algorithm itself is a way of converting an arbitrary field shape defined by an MLC to a superposition of square fields. It is likely that the algorithm has systematic errors when calculating fields with certain shape characteristics. It is also possible that plan optimization commonly results in site specific field shapes, such as a long thin MLC opening that sweeps across the field for chest wall treatments. It is therefore possible that the observed systematic offsets appear as a function of anatomical site due to errors in calculating the fields commonly used to treat them. A method for investigating this is presented in Section 4.3.

Conversely, MLC configurations for a given patient geometry can vary for each optimization. This, along with the large number of control points for each IMRT plan, makes it difficult to associate certain control point MLC configurations with an anatomical site. Since the conversion process is the same regardless of site, it is safe to assume any errors in this process would appear in all calculations as a baseline systematic offset.

Another assumption is the beam is perpendicularly incident on a flat phantom geometry. The majority of patient external contours are convex, so more scattering material than is present is assumed, increasing the algorithm dose. This approximation is probably reasonable for sites with slowly-varying external contours such as in prostate treatment plans. However, superficial sites, such as for the chest wall, may exhibit more changes in scatter which result in worse agreement. This was previously demonstrated in the results for TomoTherapy second check calculations.[18]

Heterogeneities are accounted for by assuming infinite slab geometry. The composition is determined by the material along the source to point ray and is incorporated in the calculations as an effective depth. Change in patient heterogeneities lateral to this ray could cause an overestimation or underestimation of dose depending on the relative density due to changes in scatter contribution.

All data tables are also measured at isocenter, with off-axis points being calculated with central axis data and an OAR which is a function of off-axis distance and depth. At our center the OAR which is measured with a 40 cm^2 field as a function of depth. This ratio has some field size dependency due to scatter contributions which is not accounted for and can lead to errors of greater than 5% for points more than 10 cm from the central axis.[20]

For the prostate the radius of curvature of the outer edges of the patient is large with little variation in the superior/inferior direction. It is also relatively homogeneous compared to other sites, the femoral heads being the main bony structures. For this work, isocenter was the point of calculation for all prostate plans. Out of the three sites, the prostate most closely agrees with the assumptions of the dose calculation formalism. The systematic underestimation of dose for this site is representative of the baseline error of the algorithm.

The neck has a much smaller radius of curvature, leading to overestimation of dose and is likely the main contributing factor to doses being higher than the prostate. The presence of the jaw can lead to an underestimation or overestimation of dose depending on the position of the point of calculation however it is not a factor in all cases. Similarly, heterogeneities can be bone or airways and their influence depends on the point of calculation and beam positions making generalizations difficult. Points of calculation are generally near isocenter where the off-axis calculations are appropriately accurate.

The chest wall plans have points of calculation that are far off-axis with the off-axis distance in the beam’s-eye-view varying as a function of beam angle. Beams with small off-axis distances will be perpendicularly incident on the patient with surface contours similar to that of the prostate. The lung will be downstream from the point for these beams so changes in scattered dose will be minimal. Beams with the largest off-axis ratios deviate significantly from the assumptions above. These beams will be obliquely incident on the chest wall and in extreme cases will be close to parallel with the surface. The chest wall has air on one side and lung on the other and can be extremely thin in certain patients, violating the infinite slab geometry, leading to an overestimation of dose.

Chapter 4 : Conclusions

4.1 Hypothesis and Aims

The hypothesis of this work was an independent monitor unit calculation algorithm using a superposition of open-field data could be used to calculate doses for SMLC and VMAT plans to within 2% for points in high-dose low gradient regions. Based on the results of the four aims, this hypothesis was not supported.

Aim 1 was to adapt the TomoTherapy independent dose calculation algorithm for calculation of dose from IMRT treatments delivered by a conventional MLC. This was done by developing a method to convert an arbitrary MLC pattern to the superposition of symmetric rectangular fields. IMRT treatments were then represented as the sum of multiple discrete field configurations called control points. The dose of each control point was calculated and then summed across the entire treatment.

Aim 2 was to obtain dosimetric data as required for input into the algorithm. Output factors of fields smaller than 3x3 cm^2 were measured due to their rapid fall off at small field sizes. An exponential fits using the smaller field sizes down to 0x0 cm^2 field size was used to extrapolate output factors for field sizes smaller than 1.5x1.5 cm^2.

Aim 3 was to compare the algorithm and the current independent calculation method, MuCheck v8.2, to Pinnacle v9.0 calculations and point dose ion chamber measurements of the test cases presented in TG-119. These test cases are designed for commissioning a clinics IMRT calculation and delivery system. The geometries are representative of those encountered in the clinic.

Aim 4 was to investigate algorithm behavior by calculating a series of patient plans. Three sites, the prostate, neck, and chest wall were calculated for five patients, each having a

SMLC and VMAT plan for a total of 30 plans. Calculations were also done using MuCheck v8.2 and both were compared against Pinnacle v9.2 calculations.

Results of Aim 3 indicate that algorithm performance is optimal in high dose, low gradient regions such as the PTV and suffers when calculating dose to critical structures. This is acceptable as calculation points for secondary checks are placed in the PTV. In Aim 4, not all plans were able to meet the 2% criteria outlined in the thesis, therefore the hypothesis was not supported. However with a mean percent error ± 95% confidence interval of -0.2% ± 3.8% for the algorithm compared to MuCheck's 0.7% ± 7.2% show that the algorithm is more accurate and noticeably more precise as a secondary check method than MuCheck. This is even without taking into account off-axis calculation points in VMAT plans for MuCheck which would significantly degrade performance.

4.2 Clinical Implementation

Algorithm performance has been demonstrated for a limited number of sites and should undergo a more rigorous commissioning process before clinical use. To implement this algorithm, a clinic would need to obtain open field beam data including TPRs, OARs, S_c, S_p, an average MLC leakage value, and the dose rate per monitor unit under normalization conditions. These data are already typically taken at time of machine commissioning and should be readily available.

Not all clinics have output factors for fields as small as were used in the input data in this work. The algorithm's reliance on output factors for field sizes smaller than 3x3-cm^2 still needs to be investigated as mentioned in Section 4.3.

The majority of patient specific data needed for plan calculation are available in DICOM treatment files and can be pulled from the TPS or a record and verify system. However, depth, effective depth, and SSD along the source to point of calculation ray for each control point are not stored in the DICOM file. In this work, this information was extracted from Pinnacle using a custom script, but a more streamlined method needs to be developed. If the DICOM CT images were also imported into a program, these values could be independently calculated.

Importing other treatment plan information such as control point dose or structure sets in addition to the CT images could have multiple advantages. Software with a user interface could be developed to allow the user to pick arbitrary calculation points and comparisons could be made on a control point basis. Cross plane profiles and possibly DVH comparisons could also be made, assuming algorithm performance outside the PTV sufficiently accurate. However, preliminary results seem to indicate that this is not the case.

4.3 Future Work

The observed systematic offsets as a function of calculation site deserve further investigation. Patient plans used in this project could all be delivered onto the same phantom geometry, recalculating with Pinnacle and the algorithm. If the site specific systematic offsets are still present in the algorithm calculations, than this indicates that the systematic errors are the results of field shapes common to each site, rather than differences in the patient geometry. This process would be further facilitated by being able to pull control point dose from Pinnacle, allowing for comparison of every field configuration instead of single beam or arc values.

Small field output factors were measured for the calculations in this work and reliance of algorithm accuracy on these values should be investigated. Are output factors for fields smaller than 3x3-cm^2 necessary, and how accurately do their values need to be known. Do actual measurements need to be taken or is there an extrapolation method based on data above a field size of 3x3-cm^2 that gives acceptable results. Ideally the algorithm should be able to function accurately without these values as the majority of institutions do not have small field output factors readily available.

Sensitivity of the algorithm to changes in the average value of MLC leakage should also be investigated. This would have the largest impact on plans that use highly shaped fields, such as in the neck, as these plans have the most area of MLC leaves not under the photon collimating jaws.

References

1 Faiz M. Khan, *The Physics of Radiation Therapy*. 4th edn (Philadelphia: Lippincott Williams & Wilkins, 2010), pp. x, 531, 30 p.

2 S. Webb, 'The Physical Basis of Imrt and Inverse Planning', *Br J Radiol,* 76 (2003), 678-89.

3 K. Otto, 'Volumetric Modulated Arc Therapy: Imrt in a Single Gantry Arc', *Med Phys,* 35 (2008), 310-7.

4 G. J. Kutcher, L. Coia, M. Gillin, W. F. Hanson, S. Leibel, R. J. Morton, J. R. Palta, J. A. Purdy, L. E. Reinstein, G. K. Svensson, and et al., 'Comprehensive Qa for Radiation Oncology: Report of Aapm Radiation Therapy Committee Task Group 40', *Med Phys,* 21 (1994), 581-618.

5 R. L. Stern, R. Heaton, M. W. Fraser, S. M. Goddu, T. H. Kirby, K. L. Lam, A. Molineu, and T. C. Zhu, 'Verification of Monitor Unit Calculations for Non-Imrt Clinical Radiotherapy: Report of Aapm Task Group 114', *Med Phys,* 38 (2011), 504-30.

6 D. A. Low, J. M. Moran, J. F. Dempsey, L. Dong, and M. Oldham, 'Dosimetry Tools and Techniques for Imrt', *Med Phys,* 38 (2011), 1313-38.

7 G. A. Ezzell, J. M. Galvin, D. Low, J. R. Palta, I. Rosen, M. B. Sharpe, P. Xia, Y. Xiao, L. Xing, and C. X. Yu, 'Guidance Document on Delivery, Treatment Planning, and Clinical Implementation of Imrt: Report of the Imrt Subcommittee of the Aapm Radiation Therapy Committee', *Med Phys,* 30 (2003), 2089-115.

8 K. Bzdusek, D. Robinson, M. Kaus, H. Friberger, and K. Eriksson, 'Smartarc: Background and Algorithmic Implementation of an Efficient Approach to Volumetric Arc Therapy Planning', *Philips White Paper* (2009).

9 N. Linthout, D. Verellen, S. Van Acker, and G. Storme, 'A Simple Theoretical Verification of Monitor Unit Calculation for Intensity Modulated Beams Using Dynamic Mini-Multileaf Collimation', *Radiother Oncol,* 71 (2004), 235-41.

10 J. H. Kung, G. T. Chen, and F. K. Kuchnir, 'A Monitor Unit Verification Calculation in Intensity Modulated Radiotherapy as a Dosimetry Quality Assurance', *Med Phys,* 27 (2000), 2226-30.

11 Y. Watanabe, 'Point Dose Calculations Using an Analytical Pencil Beam Kernel for Imrt Plan Checking', *Phys Med Biol,* 46 (2001), 1031-8.

12 A. Boyer, L. Xing, C. M. Ma, B. Curran, R. Hill, A. Kania, and A. Bleier, 'Theoretical Considerations of Monitor Unit Calculations for Intensity Modulated Beam Treatment Planning', *Med Phys,* 26 (1999), 187-95.

13 Y. Yang, L. Xing, J. G. Li, J. Palta, Y. Chen, G. Luxton, and A. Boyer, 'Independent Dosimetric Calculation with Inclusion of Head Scatter and Mlc Transmission for Imrt', *Med Phys,* 30 (2003), 2937-47.

14 L. Xing, Y. Chen, G. Luxton, J. G. Li, and A. L. Boyer, 'Monitor Unit Calculation for an Intensity Modulated Photon Field by a Simple Scatter-Summation Algorithm', *Phys Med Biol,* 45 (2000), N1-7.

15 X. Chen, N. J. Yue, W. Chen, C. B. Saw, D. E. Heron, D. Stefanik, R. Antemann, and M. S. Huq, 'A Dose Verification Method Using a Monitor Unit Matrix for Dynamic Imrt on Varian Linear Accelerators', *Phys Med Biol,* 50 (2005), 5641-52.

16 C. M. Ma, T. Pawlicki, S. B. Jiang, J. S. Li, J. Deng, E. Mok, A. Kapur, L. Xing, L. Ma, and A. L. Boyer, 'Monte Carlo Verification of Imrt Dose Distributions from a Commercial Treatment Planning Optimization System', *Phys Med Biol,* 45 (2000), 2483-95.

17 J. Fan, J. Li, L. Chen, S. Stathakis, W. Luo, F. Du Plessis, W. Xiong, J. Yang, and C. M. Ma, 'A Practical Monte Carlo Mu Verification Tool for Imrt Quality Assurance', *Phys Med Biol,* 51 (2006), 2503-15.

18 J. P. Gibbons, K. Smith, D. Cheek, and I. Rosen, 'Independent Calculation of Dose from a Helical Tomotherapy Unit', *J Appl Clin Med Phys,* 10 (2009), 2772.

19 G. A. Ezzell, J. W. Burmeister, N. Dogan, T. J. LoSasso, J. G. Mechalakos, D. Mihailidis, A. Molineu, J. R. Palta, C. R. Ramsey, B. J. Salter, J. Shi, P. Xia, N. J. Yue, and Y. Xiao, 'Imrt Commissioning: Multiple Institution Planning and Dosimetry Comparisons, a Report from Aapm Task Group 119', *Med Phys,* 36 (2009), 5359-73.

20 J. P. Gibbons, J. Antolak, D. S. Followill, M. S. Huq, E. E. Klein, K. L. Lam, J. Palta, D. M. Roback, M Reid, and Faiz M. Khan, 'Monitor Unit Calculations for External Photon and Electron Beams: Report of the Aapm Radiation Therapy Committee Task Group No. 71', (Submitted to *Med Phys* 2013).

21 M. J. Day, 'A Note on the Calculation of Dose in X-Ray Fields', *Br J Radiol,* 23 (1950), 368-9.

22 E.G.A. Aird, British Institute of Radiology, Institution of Physics, Engineering in Medicine, and Biology, *Central Axis Depth Dose Data for Use in Radiotherapy, 1996: A Survey of Depth Doses and Related Data Measured in Water or Equivalent Media*British Institute of Radiology, 1996).

23 T. C. Zhu, A. Ahnesjo, K. L. Lam, X. A. Li, C. M. Ma, J. R. Palta, M. B. Sharpe, B. Thomadsen, and R. C. Tailor, 'Report of Aapm Therapy Physics Committee Task Group 74: In-Air Output Ratio, Sc, for Megavoltage Photon Beams', *Med Phys,* 36 (2009), 5261-91.

24 J. P. Gibbons, ed., *Monitor Unit Calculations for External Photon and Electron Beams* (Middleton, WI: Advanced Medical Publishing, Inc, 2000).

25 G. M. Mancuso, J. D. Fontenot, J. P. Gibbons, and B. C. Parker, 'Comparison of Action Levels for Patient-Specific Quality Assurance of Intensity Modulated Radiation Therapy and Volumetric Modulated Arc Therapy Treatments', *Med Phys,* 39 (2012), 4378-85.

26 G M Mancuso, 'Evaluation of Volumetric Modulated Arc Therapy (Vmat) Patient Specific Quality Assurance', *LSU Electronic Thesis & Dissertation Collection* (2011).

Appendix A: Order of Superposition Illustrations

The ± operators in Equation 2.4 take on different vales based on the position of the point of calculation relative to the leaf gap being calculated in the beam's-eye-view. The point can be horizontally or vertically, inside or outside the leaf gap. This appendix contains illustrations of the four possible cases with their equations. Though unlikely, if the point of calculation is exactly on the boundary between two cases, the equations reduce to be equivalent since the dimension of some of the fields becomes zero. In the figures below the point of calculation is marked by the black dot and the single leaf gap is being calculated. The OAR weighting term from Equation 2.4 is denoted here as f_{OAR}.

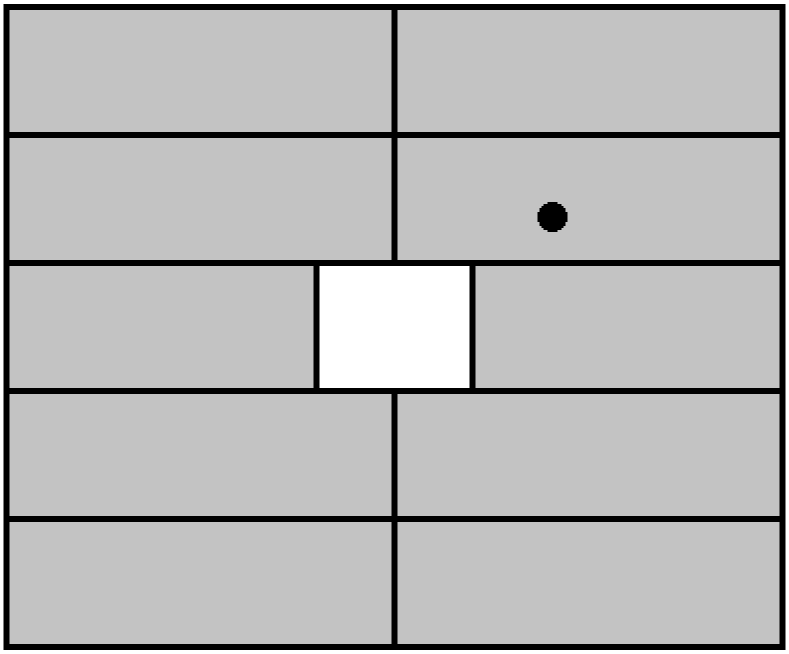

Figure A.1: Point of calculation positioning case 1.

$$D_g = f_{OAR} \cdot [(D_A - D_B) - (D_C - D_D)]$$

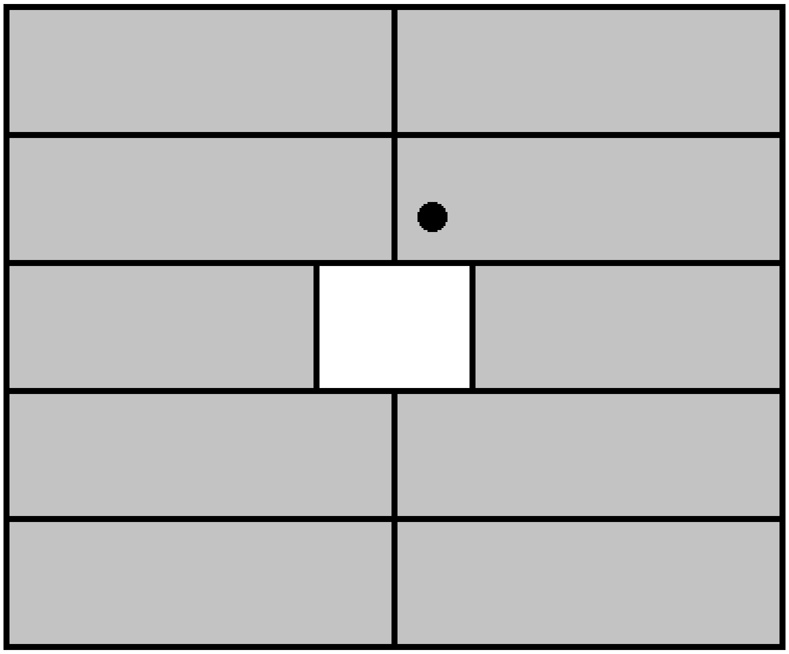

Figure A.2: Point of calculation positioning case 2.

$$D_g = f_{OAR} \cdot [(D_A - D_B) + (D_C - D_D)]$$

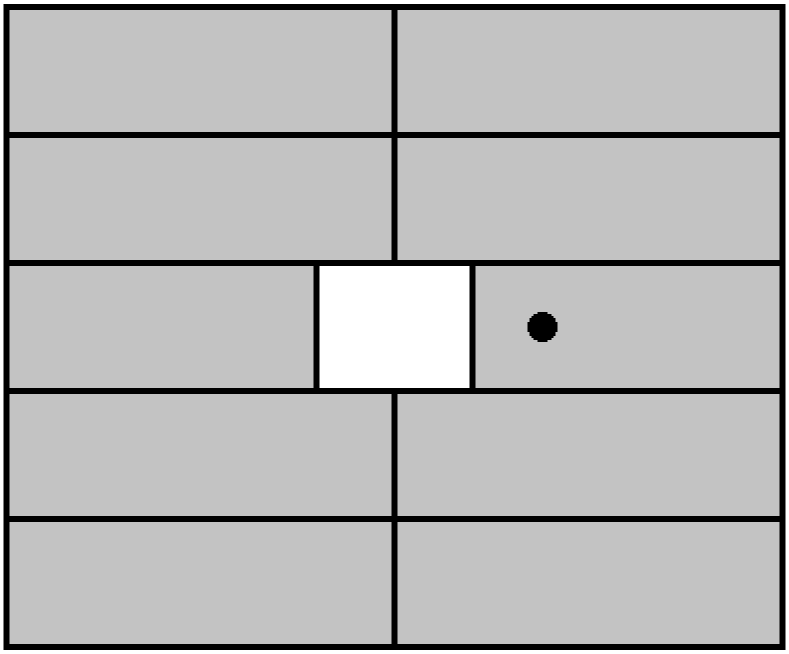

Figure A.3: Point of calculation positioning case 3.

$$D_g = f_{OAR} \cdot [(D_A + D_B) - (D_C + D_D)]$$

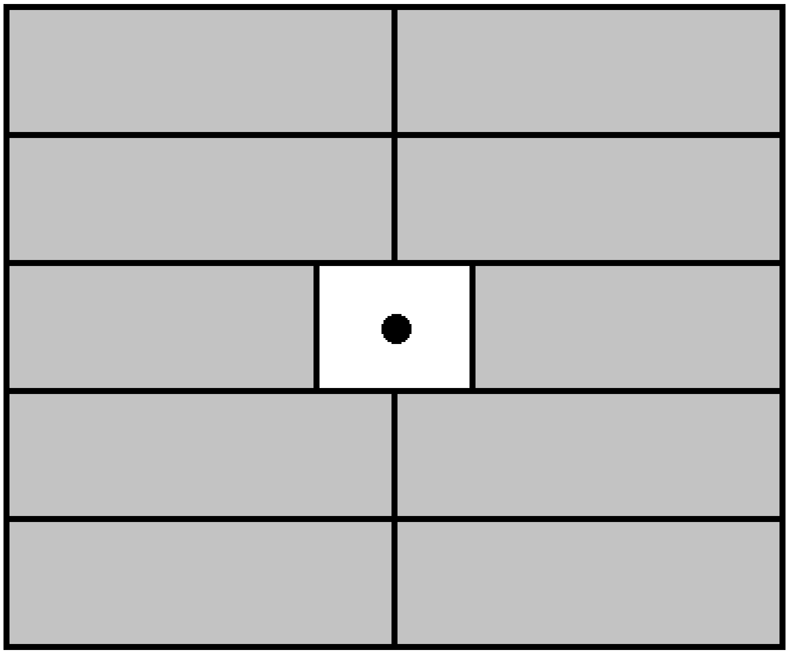

Figure A.4: Point of calculation positioning case 4.

$$D_g = f_{OAR} \cdot [(D_A + D_B) + (D_C + D_D)]$$

Appendix B: Open Field Data Used By Algorithm

This appendix contains all open field data as input into the algorithm for calculations in this work.

Table B.1: Output Factors input into algorithm.

6 MV Photons, Output Factors		
Field Size	S_c	S_p
0.0 x 0.0	0.000	0.000
0.1 x 0.1	0.242645	0.10783
0.2 x 0.2	0.423511	0.202928
0.3 x 0.3	0.558333	0.286742
0.4 x 0.4	0.658833	0.360612
0.5 x 0.5	0.733749	0.425717
0.6 x 0.6	0.789593	0.483097
0.7 x 0.7	0.83122	0.53367
0.8 x 0.8	0.86225	0.578242
0.9 x 0.9	0.885381	0.617525
1.0 x 1.0	0.902623	0.652148
1.1 x 1.1	0.915476	0.682662
1.2 x 1.2	0.925056	0.709556
1.3 x 1.3	0.932198	0.733259
1.4 x 1.4	0.937522	0.75415
1.5 x 1.5	0.941	0.768
1.67 x 1.67	0.947	0.806
2.0 x 2.0	0.950	0.834
2.5 x 2.5	0.955	0.863
3.0 x 3.0	0.957	0.880
4.0 x 4.0	0.968	0.906
5.0 x 5.0	0.975	0.922
7.5 x 7.5	0.988	0.966
10.0 x 10.0	1.000	1.000
15.0 x 15.0	1.015	1.042
20.0 x 20.0	1.024	1.073
25.0 x 25.0	1.029	1.091
30.0 x 30.0	1.034	1.106
34.0 x 34.0	1.035	1.114
40.0 x 40.0	1.033	1.125

Table B.2: Off-Axis ratios input into algorithm.

6 MV Photons, Off-Axis Ratios

OAD* [cm]	Depth [cm]					
	1.6	5	10	15	20	25
0	1.000	1.000	1.000	1.000	1.000	1.000
1	1.002	1.004	1.005	1.007	1.000	1.003
2	1.008	1.009	1.008	1.007	1.004	1.005
3	1.013	1.011	1.014	1.012	1.008	1.006
4	1.019	1.018	1.016	1.012	1.006	1.004
5	1.019	1.020	1.018	1.013	1.006	1.000
6	1.021	1.017	1.015	1.012	1.002	0.995
7	1.024	1.020	1.016	1.009	0.998	0.992
8	1.033	1.026	1.019	1.008	0.998	0.990
9	1.038	1.032	1.023	1.011	0.994	0.985
10	1.044	1.035	1.025	1.008	0.992	0.977
11	1.044	1.035	1.022	1.004	0.983	0.969
12	1.046	1.035	1.019	0.997	0.977	0.955
13	1.043	1.034	1.014	0.990	0.962	0.941
14	1.047	1.033	1.009	0.979	0.952	0.926
15	1.047	1.031	1.004	0.965	0.933	0.910
16	1.044	1.023	0.990	0.944	0.906	0.888
17	1.039	1.017	0.976	0.922	0.890	0.860
18	1.034	1.002	0.953	0.902	0.859	0.827
19	1.019	0.980	0.920	0.860	0.817	0.779
20	0.573	0.538	0.518	0.495	0.516	0.437

*Off Axis Distance is projected to 100 cm from souce. Data was taken from normalized profiles measured for the maximum square field size

Table B.3: Tissue Phantom Ratios for input into the algorithm. Field Sizes 3x3 cm^2 to 14x14 cm^2.

6 MV Photons, Tissue Phantom Ratios												
Field Size Depth [cm]	3 x 3	4 x 4	5 x 5	6 x 6	7 x 7	8 x 8	9 x 9	10 x 10	11 x 11	12 x 12	13 x 13	14 x 14
0.0	0.547	0.561	0.573	0.585	0.597	0.607	0.618	0.628	0.637	0.646	0.654	0.661
0.5	1.073	1.067	1.062	1.057	1.054	1.051	1.049	1.047	1.046	1.045	1.045	1.045
1.0	1.308	1.293	1.279	1.266	1.255	1.245	1.235	1.227	1.219	1.213	1.207	1.202
1.5	1.383	1.363	1.338	1.319	1.304	1.290	1.280	1.271	1.263	1.253	1.250	1.246
2.0	1.379	1.359	1.337	1.320	1.304	1.290	1.279	1.270	1.261	1.250	1.246	1.240
2.5	1.362	1.343	1.323	1.307	1.292	1.279	1.269	1.260	1.251	1.241	1.237	1.231
3.0	1.340	1.324	1.303	1.287	1.273	1.261	1.251	1.242	1.235	1.226	1.223	1.219
3.5	1.317	1.303	1.285	1.270	1.258	1.246	1.237	1.229	1.222	1.213	1.211	1.206
4.0	1.291	1.279	1.264	1.250	1.238	1.228	1.219	1.211	1.204	1.196	1.194	1.190
4.5	1.267	1.257	1.242	1.230	1.220	1.211	1.204	1.198	1.192	1.184	1.182	1.178
5.0	1.238	1.230	1.219	1.209	1.201	1.192	1.186	1.179	1.173	1.165	1.164	1.160
5.5	1.214	1.207	1.197	1.188	1.180	1.173	1.167	1.161	1.156	1.150	1.150	1.147
6.0	1.185	1.181	1.173	1.166	1.160	1.154	1.149	1.145	1.141	1.136	1.133	1.130
6.5	1.160	1.157	1.151	1.145	1.140	1.134	1.130	1.126	1.122	1.120	1.118	1.116
7.0	1.139	1.135	1.129	1.123	1.119	1.115	1.112	1.109	1.106	1.104	1.102	1.100
7.5	1.115	1.112	1.106	1.102	1.098	1.095	1.093	1.091	1.089	1.087	1.085	1.083
8.0	1.092	1.089	1.084	1.080	1.077	1.075	1.073	1.071	1.070	1.068	1.067	1.065
8.5	1.069	1.068	1.064	1.060	1.057	1.055	1.054	1.053	1.052	1.052	1.051	1.051
9.0	1.046	1.045	1.042	1.039	1.037	1.036	1.036	1.035	1.035	1.035	1.034	1.034
9.5	1.023	1.023	1.022	1.022	1.021	1.020	1.020	1.019	1.018	1.018	1.018	1.018
10.0	1.000	1.000	1.000	1.000	1.000	1.000	1.000	1.000	1.000	1.000	1.000	1.000
10.5	0.980	0.979	0.978	0.978	0.978	0.979	0.981	0.981	0.982	0.983	0.984	0.985
11.0	0.959	0.956	0.955	0.956	0.957	0.958	0.962	0.962	0.964	0.965	0.966	0.967
11.5	0.938	0.938	0.936	0.936	0.938	0.939	0.943	0.944	0.946	0.949	0.950	0.952
12.0	0.917	0.917	0.920	0.923	0.924	0.926	0.929	0.929	0.930	0.932	0.934	0.936
12.5	0.897	0.897	0.899	0.902	0.905	0.907	0.911	0.912	0.914	0.917	0.919	0.921
13.0	0.880	0.878	0.879	0.883	0.885	0.888	0.892	0.893	0.896	0.898	0.901	0.903
13.5	0.861	0.861	0.863	0.867	0.870	0.873	0.878	0.880	0.883	0.885	0.888	0.890
14.0	0.839	0.842	0.844	0.846	0.850	0.853	0.858	0.860	0.864	0.867	0.870	0.872
14.5	0.825	0.826	0.828	0.831	0.834	0.838	0.843	0.844	0.847	0.851	0.857	0.858
15.0	0.806	0.805	0.808	0.812	0.816	0.820	0.825	0.827	0.831	0.835	0.842	0.843
15.5	0.790	0.791	0.794	0.797	0.800	0.804	0.810	0.812	0.816	0.820	0.826	0.828
16.0	0.776	0.775	0.778	0.781	0.785	0.788	0.794	0.796	0.800	0.804	0.811	0.812
16.5	0.756	0.756	0.758	0.762	0.766	0.770	0.776	0.779	0.784	0.789	0.795	0.797
17.0	0.738	0.738	0.742	0.748	0.752	0.757	0.763	0.765	0.769	0.773	0.780	0.782
17.5	0.724	0.725	0.728	0.732	0.737	0.741	0.748	0.751	0.755	0.760	0.766	0.768
18.0	0.711	0.710	0.711	0.714	0.719	0.724	0.731	0.735	0.742	0.748	0.755	0.757
18.5	0.693	0.691	0.695	0.702	0.708	0.713	0.719	0.722	0.727	0.732	0.738	0.741
19.0	0.681	0.682	0.684	0.687	0.692	0.697	0.704	0.707	0.713	0.719	0.725	0.727
19.5	0.667	0.664	0.667	0.673	0.678	0.683	0.690	0.693	0.699	0.704	0.711	0.713
20.0	0.652	0.651	0.654	0.659	0.664	0.669	0.676	0.680	0.685	0.691	0.697	0.700
21.0	0.624	0.619	0.622	0.629	0.635	0.641	0.649	0.653	0.659	0.665	0.672	0.676
22.0	0.598	0.595	0.599	0.606	0.612	0.617	0.624	0.628	0.633	0.639	0.646	0.650
23.0	0.574	0.572	0.575	0.579	0.585	0.590	0.597	0.603	0.608	0.614	0.623	0.627
24.0	0.551	0.549	0.553	0.560	0.566	0.572	0.579	0.583	0.587	0.593	0.599	0.604
25.0	0.528	0.525	0.530	0.537	0.544	0.550	0.556	0.561	0.565	0.569	0.576	0.581
26.0	0.511	0.507	0.511	0.517	0.523	0.529	0.535	0.540	0.544	0.549	0.556	0.561
27.0	0.490	0.487	0.492	0.499	0.506	0.511	0.517	0.521	0.524	0.529	0.534	0.539
28.0	0.469	0.464	0.466	0.472	0.478	0.484	0.490	0.496	0.500	0.506	0.513	0.519
29.0	0.450	0.447	0.450	0.454	0.459	0.464	0.470	0.475	0.479	0.484	0.491	0.497
30.0	0.431	0.428	0.430	0.434	0.440	0.444	0.451	0.455	0.459	0.465	0.472	0.477

Table B.4: Tissue Phantom Ratios for input into the algorithm. Field Sizes 15x15 cm^2 to 28x28 cm^2.

6 MV Photons, Tissue Phantom Ratios											
Field Size Depth [cm]	15 x 15	16 x 16	17 x 17	18 x 18	19 x 19	20 x 20	21 x 21	22 x 22	24 x 24	26 x 26	28 x 28
0.0	0.668	0.675	0.681	0.686	0.691	0.696	0.700	0.703	0.708	0.711	0.712
0.5	1.046	1.047	1.048	1.050	1.052	1.054	1.056	1.058	1.062	1.066	1.069
1.0	1.198	1.194	1.191	1.188	1.186	1.184	1.183	1.181	1.180	1.179	1.178
1.5	1.241	1.237	1.232	1.226	1.221	1.217	1.212	1.209	1.205	1.202	1.198
2.0	1.235	1.230	1.226	1.221	1.217	1.213	1.208	1.205	1.203	1.199	1.196
2.5	1.226	1.221	1.216	1.211	1.206	1.202	1.197	1.194	1.191	1.189	1.187
3.0	1.215	1.210	1.205	1.199	1.194	1.189	1.185	1.181	1.178	1.176	1.174
3.5	1.202	1.198	1.193	1.188	1.183	1.179	1.176	1.173	1.172	1.170	1.166
4.0	1.186	1.182	1.179	1.175	1.171	1.168	1.165	1.163	1.162	1.161	1.157
4.5	1.174	1.170	1.166	1.161	1.158	1.154	1.151	1.148	1.147	1.145	1.143
5.0	1.157	1.154	1.151	1.148	1.146	1.144	1.142	1.138	1.136	1.133	1.130
5.5	1.145	1.142	1.139	1.135	1.132	1.129	1.125	1.122	1.120	1.118	1.117
6.0	1.127	1.124	1.121	1.119	1.116	1.114	1.112	1.108	1.106	1.103	1.103
6.5	1.114	1.113	1.110	1.107	1.104	1.101	1.099	1.096	1.094	1.093	1.092
7.0	1.098	1.096	1.093	1.090	1.087	1.084	1.081	1.078	1.079	1.079	1.079
7.5	1.081	1.079	1.077	1.075	1.074	1.072	1.070	1.068	1.068	1.068	1.068
8.0	1.064	1.063	1.061	1.059	1.058	1.056	1.055	1.054	1.054	1.055	1.055
8.5	1.051	1.050	1.049	1.048	1.046	1.045	1.043	1.042	1.042	1.043	1.042
9.0	1.033	1.033	1.032	1.032	1.031	1.030	1.029	1.029	1.029	1.029	1.028
9.5	1.018	1.018	1.018	1.017	1.016	1.015	1.014	1.013	1.014	1.014	1.015
10.0	1.000	1.000	1.000	1.000	1.000	1.000	1.000	1.000	1.000	1.000	1.000
10.5	0.986	0.986	0.986	0.986	0.986	0.986	0.986	0.986	0.986	0.986	0.987
11.0	0.968	0.968	0.969	0.969	0.969	0.969	0.969	0.970	0.971	0.972	0.973
11.5	0.953	0.954	0.955	0.955	0.956	0.956	0.956	0.956	0.956	0.957	0.959
12.0	0.938	0.939	0.941	0.941	0.941	0.941	0.940	0.940	0.941	0.943	0.945
12.5	0.923	0.924	0.926	0.926	0.926	0.926	0.926	0.926	0.927	0.929	0.931
13.0	0.905	0.907	0.909	0.910	0.911	0.912	0.912	0.913	0.915	0.917	0.919
13.5	0.891	0.893	0.895	0.896	0.898	0.900	0.901	0.903	0.905	0.907	0.908
14.0	0.875	0.877	0.878	0.880	0.882	0.883	0.885	0.886	0.888	0.889	0.891
14.5	0.861	0.864	0.867	0.869	0.871	0.872	0.873	0.874	0.875	0.877	0.878
15.0	0.847	0.850	0.853	0.855	0.856	0.857	0.858	0.859	0.860	0.863	0.865
15.5	0.832	0.835	0.838	0.840	0.842	0.843	0.844	0.845	0.847	0.849	0.852
16.0	0.816	0.819	0.823	0.825	0.827	0.829	0.831	0.832	0.835	0.838	0.841
16.5	0.800	0.804	0.807	0.809	0.812	0.814	0.816	0.818	0.821	0.825	0.828
17.0	0.786	0.789	0.793	0.796	0.798	0.801	0.803	0.805	0.808	0.812	0.815
17.5	0.772	0.776	0.779	0.782	0.784	0.787	0.789	0.792	0.797	0.800	0.804
18.0	0.761	0.765	0.768	0.771	0.773	0.775	0.777	0.779	0.783	0.785	0.787
18.5	0.745	0.749	0.753	0.756	0.759	0.762	0.765	0.767	0.772	0.774	0.777
19.0	0.731	0.735	0.738	0.741	0.745	0.748	0.751	0.754	0.760	0.762	0.765
19.5	0.717	0.721	0.725	0.728	0.731	0.735	0.738	0.741	0.747	0.750	0.753
20.0	0.704	0.708	0.712	0.716	0.719	0.723	0.726	0.729	0.735	0.738	0.741
21.0	0.680	0.684	0.688	0.692	0.695	0.699	0.702	0.705	0.710	0.713	0.717
22.0	0.655	0.660	0.665	0.669	0.673	0.676	0.679	0.681	0.686	0.689	0.693
23.0	0.633	0.638	0.643	0.648	0.652	0.654	0.656	0.658	0.662	0.665	0.669
24.0	0.607	0.611	0.615	0.619	0.623	0.626	0.630	0.633	0.640	0.644	0.649
25.0	0.584	0.589	0.593	0.597	0.601	0.605	0.609	0.612	0.619	0.624	0.629
26.0	0.564	0.568	0.573	0.577	0.581	0.586	0.590	0.593	0.601	0.605	0.609
27.0	0.542	0.547	0.551	0.555	0.559	0.563	0.567	0.570	0.577	0.582	0.587
28.0	0.523	0.528	0.533	0.538	0.543	0.547	0.551	0.554	0.561	0.565	0.568
29.0	0.502	0.507	0.512	0.517	0.522	0.526	0.529	0.532	0.538	0.542	0.547
30.0	0.482	0.487	0.492	0.497	0.502	0.506	0.510	0.513	0.521	0.526	0.531

Table B.5: Tissue Phantom Ratios for input into the algorithm. Field Sizes 30x30 cm^2 to 40x40 cm^2.

	6 MV Photons, Tissue Phantom Ratios					
Field Size Depth [cm]	30 x 30	32 x 32	34 x 34	36 x 36	38 x 38	40 x 40
0.0	0.711	0.707	0.702	0.695	0.685	0.674
0.5	1.071	1.072	1.071	1.068	1.063	1.054
1.0	1.177	1.175	1.172	1.167	1.160	1.150
1.5	1.195	1.192	1.189	1.185	1.180	1.175
2.0	1.193	1.190	1.186	1.181	1.176	1.170
2.5	1.185	1.182	1.177	1.173	1.168	1.163
3.0	1.173	1.170	1.166	1.163	1.160	1.157
3.5	1.163	1.159	1.157	1.155	1.151	1.147
4.0	1.153	1.150	1.147	1.144	1.141	1.137
4.5	1.141	1.138	1.136	1.134	1.131	1.128
5.0	1.128	1.127	1.126	1.125	1.122	1.117
5.5	1.116	1.116	1.114	1.112	1.109	1.106
6.0	1.103	1.104	1.101	1.098	1.096	1.093
6.5	1.091	1.089	1.088	1.087	1.085	1.082
7.0	1.079	1.079	1.077	1.075	1.073	1.071
7.5	1.068	1.067	1.066	1.064	1.062	1.060
8.0	1.055	1.054	1.052	1.051	1.049	1.048
8.5	1.041	1.039	1.039	1.040	1.040	1.039
9.0	1.028	1.027	1.027	1.027	1.027	1.026
9.5	1.015	1.014	1.014	1.013	1.013	1.012
10.0	1.000	1.000	1.000	1.000	1.000	1.000
10.5	0.988	0.989	0.989	0.989	0.988	0.987
11.0	0.974	0.975	0.976	0.976	0.976	0.975
11.5	0.961	0.963	0.964	0.964	0.963	0.962
12.0	0.945	0.945	0.946	0.948	0.950	0.950
12.5	0.934	0.936	0.938	0.938	0.937	0.937
13.0	0.922	0.924	0.925	0.925	0.924	0.924
13.5	0.909	0.910	0.912	0.913	0.915	0.915
14.0	0.893	0.895	0.897	0.900	0.903	0.904
14.5	0.881	0.884	0.888	0.890	0.891	0.892
15.0	0.869	0.872	0.876	0.877	0.877	0.877
15.5	0.856	0.859	0.862	0.864	0.866	0.868
16.0	0.843	0.846	0.848	0.850	0.852	0.854
16.5	0.831	0.834	0.836	0.838	0.840	0.842
17.0	0.818	0.821	0.824	0.825	0.826	0.827
17.5	0.807	0.810	0.813	0.814	0.816	0.817
18.0	0.790	0.794	0.797	0.801	0.803	0.806
18.5	0.780	0.785	0.789	0.792	0.793	0.794
19.0	0.767	0.771	0.775	0.779	0.782	0.785
19.5	0.756	0.759	0.763	0.766	0.769	0.771
20.0	0.744	0.748	0.753	0.756	0.759	0.762
21.0	0.721	0.725	0.729	0.732	0.734	0.736
22.0	0.696	0.700	0.704	0.707	0.710	0.713
23.0	0.673	0.678	0.683	0.688	0.691	0.693
24.0	0.653	0.658	0.662	0.666	0.670	0.673
25.0	0.633	0.638	0.641	0.645	0.648	0.651
26.0	0.613	0.616	0.620	0.624	0.628	0.632
27.0	0.591	0.596	0.600	0.604	0.608	0.611
28.0	0.571	0.575	0.580	0.585	0.590	0.593
29.0	0.553	0.558	0.563	0.567	0.571	0.574
30.0	0.536	0.542	0.546	0.550	0.553	0.556

Appendix C: Results of TG-119 Phantom Calculations

This appendix contains full results of all TG-119 plans calculated according to Aim 3. Table C.1 to Table C.4 show the results of both calculation methods as compared against ion chamber measurements.

Table C.5 to Table C.8 show the results of both calculation methods as compared against calculations of the Pinnacle TPS. Calculations below 2% error are highlighted green, 3% to 5% are yellow, and above 5% are red.

Table C.1: Multitarget plans compared to ion chamber measurements.

Multitarget Plans						
Modality	Point	Measured Dose (cGy) [Mean ± SD]	MuCheck Dose (cGy)	% Error	Algorithm Dose (cGy)	% Error
SMLC	50 Gy	213.9 ± 0.3	212.1	-0.8	211.7	-1.4
	25 Gy	118.5 ± 0.9	111.1	-6.2	119.9	-1.5
	12.5 Gy	59.8 ± 0.5	51.2	-14.3	60.7	-5.5
VMAT	50 Gy	219.0 ± 0.2	211.6	-3.4	218.5	0.0
	25 Gy	108.0 ± 0.2	112.0	3.7	106.2	-1.5
	12.5 Gy	53.7 ± 0.2	50.2	-6.4	49.7	-11.5

Table C.2: Mock Prostate plans compared to ion chamber measurements.

Mock Prostate Plans						
Modality	Point	Measured Dose (cGy) [Mean ± SD]	MuCheck Dose (cGy)	% Error	Algorithm Dose (cGy)	% Error
SMLC	PTV	182.6 ± 0.2	181.4	-0.7	180.3	-2.0
	Rectum	134.4 ± 0.5	142.1	5.8	126.2	-5.0
	Bladder	138.8 ± 0.8	-	-	140.0	-1.0
VMAT	PTV	184.3 ± 0.3	181.6	-1.5	183.0	-1.2
	Rectum	144 ± 0.3	181.9	26.3	141.4	-1.3
	Bladder	129.4 ± 0.8	183.2	41.6	131.2	-4.0

Table C.3: Mock Neck plans compared to ion chamber measurements.

Mock Neck Plans						
Modality	Point	Measured Dose (cGy) [Mean ± SD]	MuCheck Dose (cGy)	% Error	Algorithm Dose (cGy)	% Error
SMLC	PTV	207.1 ± 0.0	205.5	-0.8	209.9	-1.5
	Spinal Cord	124.1 ± 1.4	146.6	18.1	118.0	-4.3
VMAT	PTV	198.0 ± 0.3	204.4	3.2	198.5	-3.7
	Spinal Cord	127.4 ± 0.9	218.8	71.7	123.3	-7.9

Table C.4: C-shape plans compared to ion chamber measurements.

C-shape Plans						
Modality	Point	Measured Dose (cGy) [Mean ± SD]	MuCheck Dose (cGy)	% Error	Algorithm Dose (cGy)	% Error
SMLC	PTV	212.0 ± 0.3	-	-	205.8	-1.0
	Core	53.2 ± 0.3	46.6	-12.4	50.3	-9.5
VMAT	PTV	202.0 ± 0.7	43.1	-78.7	204.9	-1.4
	Core	44.0 ± 0.3	16.6	-62.2	41.8	-12.6

Table C.5: Multitarget plans compared to Pinnacle calculations.

Multitarget Plans						
Modality	Point	Pinnacle Dose (cGy)	MuCheck Dose (cGy)	% Error	Algorithm Dose (cGy)	% Error
SMLC	50 Gy	214.7	212.1	-1.2	211.7	-1.1
	25 Gy	121.7	111.1	-8.6	119.9	1.2
	12.5 Gy	64.3	51.2	-20.3	60.7	1.6
VMAT	50 Gy	218.6	211.6	-3.2	218.5	-0.2
	25 Gy	107.8	112.0	3.9	106.2	-1.7
	12.5 Gy	56.2	50.2	-10.6	49.7	-7.4

Table C.6: Mock Prostate plans compared to Pinnacle calculations.

Mock Prostate Plans						
Modality	Point	Pinnacle Dose (cGy)	MuCheck Dose (cGy)	% Error	Algorithm Dose (cGy)	% Error
SMLC	PTV	184.0	181.4	-1.4	180.3	-1.3
	Rectum	132.9	142.1	7.0	126.2	-6.1
	Bladder	141.3	-	-	140.0	0.8
VMAT	PTV	185.3	181.6	-2.0	183.0	-0.7
	Rectum	143.3	181.9	27.0	141.4	-1.8
	Bladder	136.7	183.2	34.1	131.2	1.4

Table C.7: Mock Neck plans compared to Pinnacle calculations.

Mock Neck Plans						
Modality	Point	Pinnacle Dose (cGy)	MuCheck Dose (cGy)	% Error	Algorithm Dose (cGy)	% Error
SMLC	PTV	213.0	205.5	-3.5	209.9	1.4
	Spinal Cord	123.3	146.6	18.9	118.0	-4.9
VMAT	PTV	206.2	204.4	-0.9	198.5	0.3
	Spinal Cord	133.9	218.8	63.4	123.3	-3.2

Table C.8: C-shape plans compared to Pinnacle calculations.

C-shape Plans						
Modality	Point	Pinnacle Dose (cGy)	MuCheck Dose (cGy)	% Error	Algorithm Dose (cGy)	% Error
SMLC	PTV	207.9	-	-	205.8	-2.9
	Core	55.6	46.6	-16.2	50.3	-5.4
VMAT	PTV	207.7	43.1	-79.3	204.9	1.4
	Core	47.8	16.6	-65.2	41.8	-5.0

Appendix D: Results of Patient Plan Calculation

This appendix full results of all patient plans as calculated according to aim 4. Table D.1 to Table D.3 show the plan dose values for both calculation methods as compared to Pinnacle. Calculations below 2% error are highlighted in green, 3% to 5% are yellow, and above 5% are red.

Table D.1: Results for patient prostate plans.

Prostate Plans					
Modality	Pinnacle Dose (cGy)	MuCheck Dose (cGy)	% Error	Algorithm Dose (cGy)	% Error
SMLC	200.5	196.4	-2.0	196.1	-2.2
	199.9	196.3	-1.8	195.2	-2.4
	200.6	194.9	-2.9	196.0	-2.3
	200.8	198.3	-1.2	198.3	-1.2
	200.7	193.3	-3.7	196.8	-1.9
VMAT	200.0	206.2	3.1	196.1	-1.9
	200.2	199.7	-0.2	195.5	-2.3
	200.1	205.1	2.5	194.6	-2.8
	199.9	204.2	2.2	196.2	-1.8
	200.1	187.6	-6.2	194.9	-2.6

Table D.2: Results for patient neck plans.

Neck Plans					
Modality	Pinnacle Dose (cGy)	MuCheck Dose (cGy)	% Error	Algorithm Dose (cGy)	% Error
SMLC	203.2	205.2	1.0	204.4	0.6
	200.2	213.3	6.5	200.5	0.2
	199.5	218.5	9.5	200.8	0.7
	200.5	198.7	-0.9	198.9	-0.8
	199.3	199.7	0.2	198.5	-0.4
VMAT	200.2	192.2	-4.0	194.5	-2.8
	200.3	181.6	-9.3	200.2	0.0
	200.0	181.3	-9.3	203.0	1.5
	204.0	228.2	11.8	201.3	-1.3
	254.3	288.0	13.2	252.4	-0.8

Table D.3: Results for patient chest wall plans.

Chest Wall Plans					
Modality	Pinnacle Dose (cGy)	MuCheck Dose (cGy)	% Error	Algorithm Dose (cGy)	% Error
SMLC	200.0	202.0	1.0	205.4	2.7
	199.9	204.3	2.2	209.7	4.9
	199.9	211.3	5.7	203.8	1.9
	200.1	197.9	-1.1	203.5	1.7
	200.0	200.3	0.2	201.9	1.0
VMAT	200.2	149.8	-25.2	202.9	1.4
	202.1	112.6	-44.3	205.8	1.8
	199.7	104.2	-47.8	203.1	1.7
	235.9	151.9	-35.6	237.3	0.6
	200.1	218.3	9.1	201.4	0.6

Vita

Adam Watts is a native of Northern Virginia and developed an interest in physics in high school. He received a B.S. in Physics from the University of Delaware in 2010 where he first learned about Medical Physics from a guest speaker. He was admitted to the Medical and Health Physics program at Louisiana State University to pursue a Master's of Medical Physics. During this time, the clinical experience gained through a partnership with Mary Bird Perkins Cancer Center has solidified his goal of becoming a clinical medical physicist.